



Dalton
Transactions

**Exploring Second Coordination Sphere Effects in Flavodiiron
Nitric Oxide Reductase Model Complexes**

Journal:	<i>Dalton Transactions</i>
Manuscript ID	DT-ART-08-2023-002828.R1
Article Type:	Paper
Date Submitted by the Author:	25-Oct-2023
Complete List of Authors:	Bracken, Abigail; University of Michigan, Department of Chemistry Dong, Hai; University of Michigan, Department of Chemistry Lengel, Michael; University of Michigan, Department of Chemistry Lehnert, Nicolai; University of Michigan, Department of Chemistry

SCHOLARONE™
Manuscripts

Exploring Second Coordination Sphere Effects in Flavodiiron Nitric Oxide Reductase Model Complexes

Abigail J. Bracken,^a Hai T. Dong,^a Michael O. Lengel,^a Nicolai Lehnert^{a,*}

^a Department of Chemistry, The University of Michigan, Ann Arbor, Michigan 48109-1055, United States

Abstract:

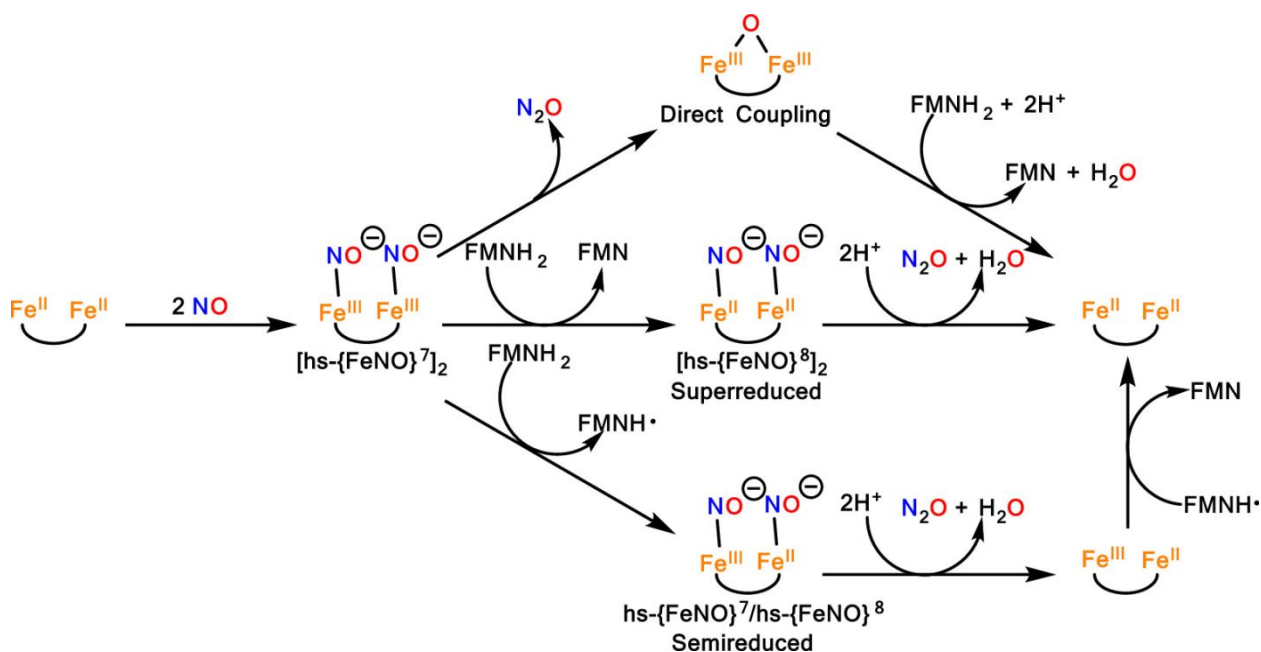
Flavodiiron nitric oxide reductases (FNORs) equip pathogens with resistance to nitric oxide (NO), an important immune defense agent in mammals, allowing these pathogens to proliferate in the human body, potentially causing chronic infections. Understanding the mechanism of how FNORs mediate the reduction of NO contributes to the greater goal of developing new therapeutic approaches against drug-resistant strains. Recent density functional theory calculations suggest that a second coordination sphere (SCS) tyrosine residue provides a hydrogen bond that is critical for the reduction of NO to N₂O at the active site of FNORs [Lu et al., *Angew. Chem. Int. Ed.* **2019**, *58*, 3795–3799]. Specifically, this network stabilizes the hyponitrite intermediate and reduces the energetic barrier for the N-N coupling step. At the same time, the role of the Fe^{•••}Fe distance and its effect on the N-N coupling step has not been fully investigated. In this study, we equipped the H[BPMP] (= 2,6-bis[[bis(2-pyridylmethyl)amino]methyl]-4-methylphenol) ligand with SCS amide groups and investigated the corresponding diiron complexes with 0 – 2 bridging acetate ligands. These amide groups can form hydrogen bonds with the bridging acetate ligand(s) and potentially the coordinated NO groups in these model complexes. At the same time, by changing the number of bridging acetate ligands, we can systematically vary the Fe^{•••}Fe distance. The reactivity of these complexes with NO was then investigated, and the formation of stable iron(II)-NO complexes was observed. Upon one-electron reduction, these NO complexes form Dinitrosyl Iron Complexes (DNICs), which were further characterized using IR and EPR spectroscopy.

1. Introduction

Nitric oxide (NO) is an important molecule that plays crucial roles in many aspects of life. Long before the discovery of NO's role in physiology, it was regarded as an environmental pollutant due to its highly toxic and corrosive properties. NO is generated from the burning of fossil fuels and is one of the main contributors to chemical smog from industrial processes, as it is toxic to humans at only 100 ppm. However, our general view of NO took a sharp turn in the 1980s after the discovery of its functions in immune defense and signaling in humans. This discovery paved the way for the Nobel Prize in Medicine in 1998.¹⁻³ At nanomolar concentrations, NO participates in signaling pathways that regulate blood pressure and are involved in nerve signal transduction in mammals.⁴⁻⁶ At higher, micromolar concentrations, NO is toxic but as a result can be used by mammals for immune defense.⁷ NO has many important biomedical applications and has promising applications in devices that can generate the gas electrochemically, allowing for the controlled release of NO in certain parts of the body.⁸⁻¹¹

Pathogenic bacteria such as *Escherichia coli*, *Desulfovibrio gigas*, *Moorella thermoacetica*, *Trichomonas vaginalis*, *Klebsiella pneumoniae*, *Salmonella typhimurium*, etc. have evolved to express Flavodiiron NO Reductases (FNORs), which can reduce NO to less toxic N₂O.¹²⁻¹⁸ Consequently, these pathogens can proliferate in the human body, causing chronic infections that are difficult to cure.¹⁹⁻²³ This highlights the significance of research on FNORs, with the long-term goal to develop new therapeutic strategies against drug resistant strains of FNOR-containing bacteria.

Scheme 1. Mechanistic Possibilities for N₂O Formation from the [hs-FeNO]⁷]₂ intermediate in FNORs. Reprinted with Permission from ref. 25. Copyright 2021 American Chemical Society.



One important piece that is missing in our understanding of FNORs is a better mechanistic picture of how FNORs reduce NO to N₂O. FNORs belong to the family of flavodiiron proteins (FDPs), which are known for their ability to reduce O₂ to water.^{24,25} FNORs are FDPs that are dedicated to NO reduction, but that are otherwise similar to other members of the FDP enzyme family.²⁵ The FNOR active site contains a nonheme diiron center, where each iron is coordinated by two histidine and one carboxylate (aspartate/glutamate) side chain. The iron centers are also bridged by both an aspartate side chain and a hydroxide group.^{12,25,26} Mechanistic studies by Kurtz and coworkers on *Thermotoga maritima* (*Tm*) FDP have provided strong evidence that FNORs reduce NO following the so-called direct NO reduction mechanism, as shown in **Scheme 1**, top.²⁷⁻²⁹ Here, the diferrrous active site of the enzyme binds two equivalents of NO first, generating the [hs-FeNO]⁷]₂ intermediate (using the Enemark-Feltham notation,³⁰ {FeNO}^{*n*}, where *n* equals the number of Fe(d) and NO(π^*) electrons – here *n* = 7; hs = high-spin). Note that for non-heme iron centers, the {FeNO}⁷ adducts are in the hs state (*S*_t = 3/2), and are best described as hs-Fe(III)-³NO⁻ type complexes, where the spins of the hs-Fe(III) (*S* = 5/2) and the ³NO⁻ (*S* = 1) are antiferromagnetically coupled.³¹⁻³³ In the rapid kinetic studies by the Kurtz group, this intermediate

is observed right before iron oxidation and N_2O release occurs.²⁹ Further evidence for this mechanism was provided by the use of deflavinated enzyme. In this case, the diferrous reactive state of *Tm* FDP can still reduce NO to N_2O , in support of the direct NO reduction mechanism.²⁸ At the same time, a number of diferrous dinitrosyl $\text{hs-}[\{\text{FeNO}\}^7]_2$ model complexes have been reported that are stable and do not mediate NO reduction.^{25,34-37} However, in these cases the $[\text{FeNO}]_2$ units can be activated by one-electron reduction to the $\text{hs-}\{\text{Fe}(\text{NO})\}^7/\text{hs-}\{\text{Fe}(\text{NO})\}^8$ state, followed by fast N_2O release, even at $-80\text{ }^\circ\text{C}$ (the semireduced mechanism in Scheme 1, bottom). These observations raise questions regarding the role of the FMN cofactor in FDPs and whether it is necessary for NO reduction in FDPs more dedicated to NO reduction than *Tm* FDP, under turnover conditions.²⁵ Another mechanistic possibility is the superreduced pathway in Scheme 1, middle, although it has so far only been observed for diiron mononitrosyl complexes.³⁸ Various FNOR model complexes have been developed to investigate the different pathways for NO reduction, some examples of which are shown in **Figure 1**, but the mechanism of N_2O formation by FNORs is still debated due to the numerous contributing factors involved in the process.³⁸⁻⁴²

Redox potential is an important factor to enabling direct NO reduction in FNOR model complexes. As shown in our previous work, we were able to activate the direct NO reduction pathway by tuning the reduction potential of the diiron core in our model complex $[\text{Fe}^{\text{II}}_2((\text{Py}_2\text{PhO}_2)\text{MP})(\text{OPr})_2]^-$.⁴¹ However, the reduction potential of this complex is around 300 mV more negative compared to FNORs, for example the enzymes from *Entamoeba histolytica* and *Escherichia coli*.^{43,44} This is also reflected by the degree of activation of the $\text{hs-}\{\text{FeNO}\}^7$ units: in model complexes, diiron centers with $\text{hs-}\{\text{FeNO}\}^7$ units with N-O stretching frequencies $\leq 1700\text{ cm}^{-1}$ are required for direct NO reduction to occur, whereas complexes with higher N-O stretching frequencies are stable, and need further activation by reduction.^{45,46} Here, the N-O stretching frequency is directly correlated with the amount of π -donation from the coordinated ${}^3\text{NO}^-$ ligand to the $\text{hs-Fe}(\text{III})$ center, where electron-rich iron centers receive less π -donation from the ${}^3\text{NO}^-$ ligand, causing a drop in the N-O stretch, a weaker Fe-NO bond, and increased radical character on the ${}^3\text{NO}^-$ ligand, which, in turn, increases their reactivity towards N-N coupling.^{25,36}

In contrast to the model complexes, the N-O stretching frequency of the $\text{hs-}[\{\text{FeNO}\}^7]_2$ intermediate in *Tm* FNOR was reported to be 1751 cm^{-1} .⁴⁷ Therefore, we hypothesize that there are other key factors at play in FNORs that enable them to mediate direct NO reduction with less activated $\text{hs-}\{\text{FeNO}\}^7$ units. One hint in this regard comes from recent mutagenesis experiments

on *Tm* FDP and computational (QM/MM) studies on the enzyme mechanism.^{27,48} Here, it is shown that hydrogen bonding residues in the second coordination sphere (SCS), specifically a conserved tyrosine residue (Y197 in *Tm* FDP; see **Scheme 2**), play a critical role in the N–N bond formation reaction that leads to the generation of a hyponitrite intermediate and ultimately N₂O release. Further mutagenesis experiments on *Tm* FDP reveal that removal of this SCS hydrogen bond donor in the Y197F variant still allows for the formation of the critical $hs\text{-}[\{\text{FeNO}\}^7]_2$ intermediate, but completely shuts down N₂O formation.²⁷

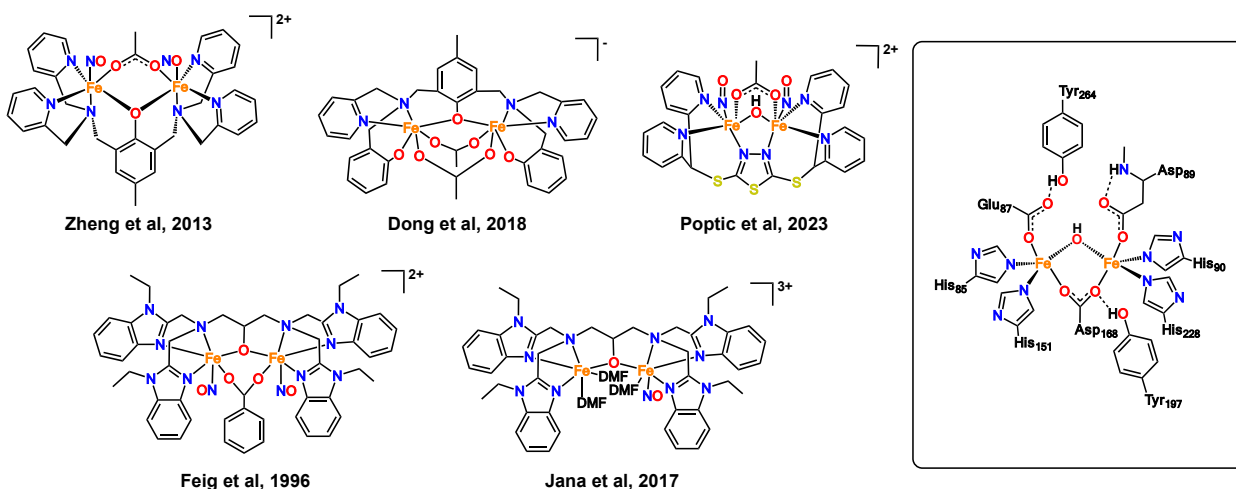
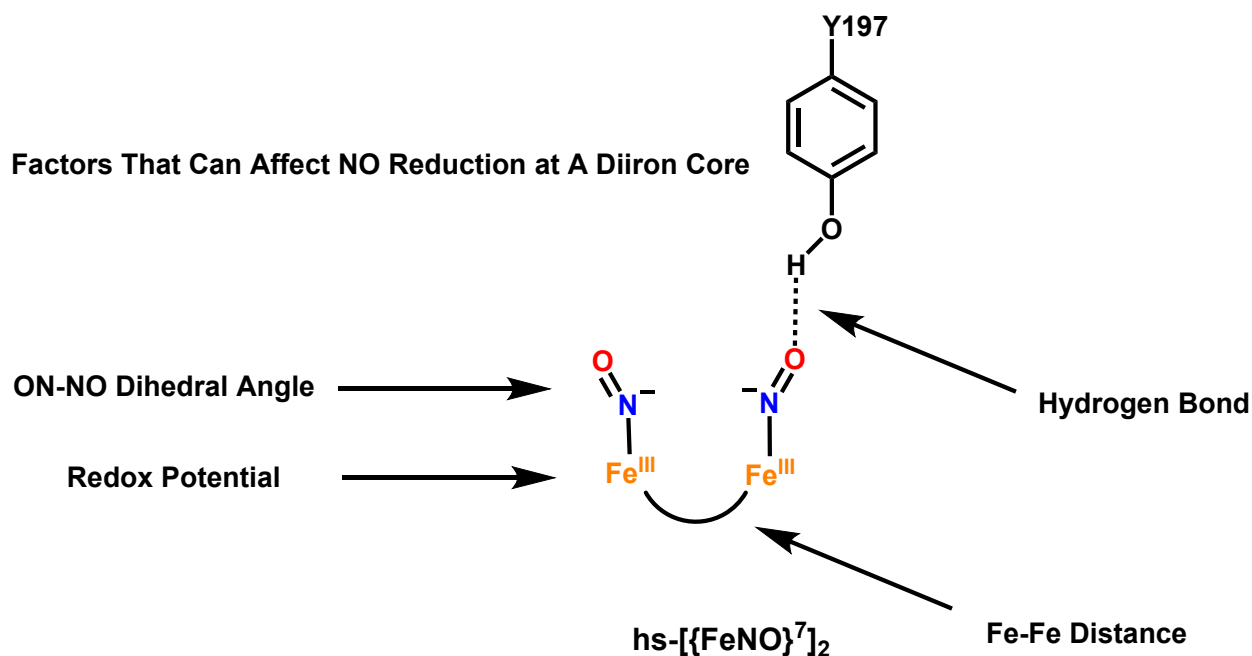


Figure 1. ChemDraw representations of previously reported model complexes (left)^{38–42} and the FNOR active site (right).²⁵

Other factors (see **Scheme 2**) that could affect the ability of a diiron core to mediate NO reduction are geometric considerations, specifically the Fe \cdots Fe distance and relative orientation of the [FeNO] units.⁴⁹ We, therefore, started a comprehensive investigation to interrogate these key features that determine the feasibility of the direct NO reduction pathway by diiron centers. In this regard, the synthesis, structural characterization, and reactivity of model complexes of FNORs with NHC(O)R (amide) type hydrogen bond donors in the SCS are reported here, along with the reactivity of these complexes towards NO. For this purpose, we previously reported on a diiron complex with the ligand H[BPMP(NHCO^tBu)₂],⁵⁰ a derivative of the H[BPMP] scaffold that we studied previously,^{34,40} and that features amide hydrogen bond donors in the SCS (note that this ligand was first reported in ref. ⁵¹). Using this ligand system, we reported a unique mononitrosyl complex, [Fe₂(BPMP(NHCO^tBu)(NCO^tBu))(OAc)(NO)](OTf) (**1(NO)**), formed through the deprotonation of one of the amide groups and subsequent coordination of its oxygen atom to one

of the iron centers.⁵⁰ In this paper, we expand our previous studies on the $\text{Fe}_2(\text{BPMP}(\text{NHCO}^t\text{Bu})_2)$ platform to further explore the importance of the bridging carboxylate ligands and potential hydrogen bonds involving the SCS amide groups for the reaction of our diiron model complexes with NO.



Scheme 2. Factors in FNORs that can affect the ability of the diiron core to mediate NO reduction.²⁵

2. Experimental Section

Reactions were generally performed using inert gas (Schlenk) techniques. All solvents were dried and freeze pump thawed to remove dioxygen and water. Preparation and handling of air sensitive materials was performed under a dinitrogen (N_2) atmosphere in an MBraun glovebox, equipped with a circulating purifier (O_2 , H_2O <0.1 ppm). Nitric oxide (99.95%) was first passed through an Ascarite II column and then a -80 °C cold trap to remove higher nitrogen oxide impurities prior to use.

Infrared spectra of solid samples were obtained using PerkinElmer BX and GX and Bruker Alpha-E FTIR spectrometer. The IR spectra of solution samples were obtained in thin-layer solution cells equipped with CaF_2 windows. Gas IR spectra were obtained using a Pike

Technologies short-path HT gas cell with 100 mm path length, equipped with CaF₂ windows, on the PerkinElmer instruments.

UV-Vis spectra were obtained using an Analytic Jena Specord S600 UV-Vis spectrometer.

¹H-NMR spectra were recorded on a Varian Inova 400 MHz instrument and referenced against residual solvent signals.

Cyclic voltammograms (CVs) were obtained on a CH instruments CHI660C electrochemical workstation using a three-component system, consisting of a glassy carbon working electrode, a platinum auxiliary electrode, and an Ag wire reference electrode. CVs were recorded in 0.1 M tetrabutylammonium triflate ([TBA](OTf)) as the supporting electrolyte in CH₂Cl₂. Potentials were corrected to the Fc⁺/Fc standard by independently measuring the ferrocenium/ferrocene couple under the same conditions (Fc⁺/Fc = 624 mV vs. SHE).

IR-Spectroelectrochemistry. IR-spectroelectrochemical (SEC-IR) experiments were conducted using a LabOmak UF-SEC thin layer cell, with Pt mesh working and counter electrodes, and an Ag wire pseudoreference electrode. Data were collected on 10 mM solutions in CH₂Cl₂ using 0.1 M [TBA](OTf) as the supporting electrolyte.

Elemental analysis: Elemental analyses were conducted by Atlantic Microlabs (Norcross, GA).

IR Gas Headspace Analysis for N₂O Detection. N₂O quantification was carried out by gas headspace analysis using infrared spectroscopy. The general protocol for gas headspace analysis was performed as previously described.⁴⁹

Generation of ¹⁵NO. ¹⁵NO gas was generated according to a previously published procedure, using either ferrocene or cobaltocene as the reductant.⁴⁹

Preparation of Compounds and Characterization. The ligand H[BPMP(NHCO^tBu)₂] was synthesized as reported in previous publications.^{50,51} ¹H-NMR (400 MHz, CDCl₃): δ 8.47 (ddd, *J* = 4.9, 1.8, 0.9 Hz, 1H), 8.22 (s, 1H), 8.07 (dd, *J* = 8.3, 0.8 Hz, 1H), 7.66 – 7.51 (m, 2H), 7.47 (dt, *J* = 7.8, 1.2 Hz, 1H), 7.14 – 7.02 (m, 3H), 4.10 (q, *J* = 7.2 Hz, 3H), 3.85 (s, 2H), 3.77 (d, *J* = 12.0 Hz, 4H), 2.25 (s, 2H), 2.03 (s, 5H), 1.30 (m, 18H).

Synthesis of [Fe₂(BPMP(NHCO^tBu)₂)(MeOH)₂](OTf)₃ (**0**). In a dinitrogen atmosphere, 1.1 equivalents of the ligand H[BPMP(NHCO^tBu)₂] were dissolved in ~3 mL of methanol. One equivalent of potassium methoxide (KOMe) was added to deprotonate the ligand, followed by two equivalents of iron(II) triflate (Fe(OTf)₂·2CH₃CN) for metallation (**Scheme 3**). The resulting

mixture was purified by first removing methanol under reduced pressure to yield a crude solid. The crude solid was redissolved in CH_2Cl_2 and filtered to remove salt byproducts. CH_2Cl_2 was then removed under reduced pressure. The solid was dissolved in THF and recrystallized via slow diffusion of diethyl ether at $-35\text{ }^\circ\text{C}$ twice to yield a greenish-brown powder. Yield. 63%. Elemental analysis calculated for $\text{C}_{48}\text{H}_{59}\text{F}_9\text{Fe}_2\text{N}_8\text{O}_{14}\text{S}_3$: Expected: C, 42.47; H, 4.40; N, 8.29 Found: C, 42.33; H, 4.32; N, 7.90. UV-Vis: 381 nm, $\epsilon = 1922\text{ M}^{-1}\text{ cm}^{-1}$.

The complex **[Fe₂(BPMP(NHCO^tBu)₂)(OAc)](OTf)₂ (1)** was synthesized according to a published procedure.⁵⁰ Elemental analysis calculated for $\text{C}_{47}\text{H}_{54}\text{F}_6\text{Fe}_2\text{N}_8\text{O}_{11}\text{S}_2$: Expected: C, 47.17; H, 4.55; N, 9.36. Found: C, 47.30; H, 4.82; N, 9.22. UV-Vis: 393 nm, $\epsilon = 1435\text{ M}^{-1}\text{ cm}^{-1}$.

Synthesis of **[Fe₂(BPMP(NHCO^tBu)₂)(OAc)₂](OTf) (2)**: Complex **2** was synthesized according to a modified, published procedure, using OTf^- as the counterion rather than PF_6^- .⁵² In a dinitrogen atmosphere, 1.1 equivalents of the ligand $\text{H}[\text{BPMP}(\text{NHCO}^t\text{Bu})_2]$ were dissolved in ~ 3 mL of methanol. One equivalent of potassium methoxide (KOMe) was added to deprotonate the ligand, followed by the addition of two equivalents of iron(II) triflate ($\text{Fe}(\text{OTf})_2 \cdot 2\text{CH}_3\text{CN}$) for metallation. The solution was allowed to stir for ~ 10 minutes before adding two equivalents of sodium acetate (NaOAc). The resulting mixture was purified by first removing methanol under reduced pressure to yield a crude solid. The crude solid was redissolved in CH_2Cl_2 and filtered to remove salt byproducts. CH_2Cl_2 was then removed under reduced pressure. The solid was dissolved in THF and recrystallized via slow diffusion of diethyl ether at $-35\text{ }^\circ\text{C}$ twice to yield an orange-brown powder, as reported in the literature.⁵² UV-Vis: 384 nm, $\epsilon = 1586\text{ M}^{-1}\text{ cm}^{-1}$.

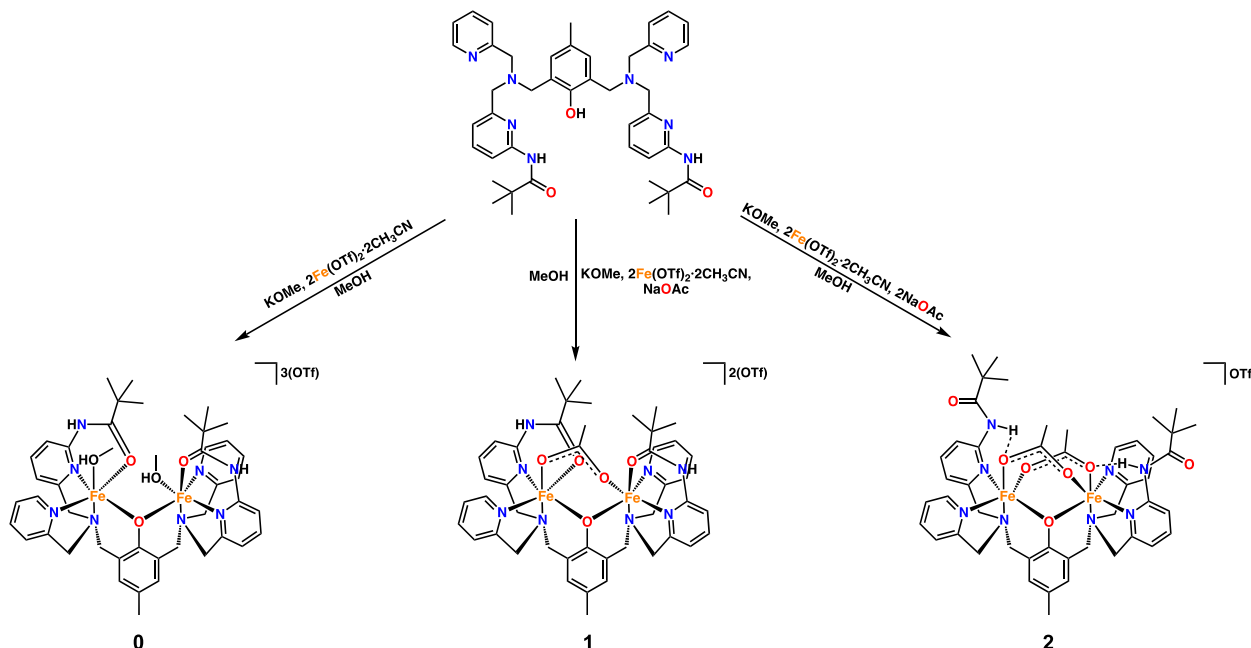
X-ray Crystallography. Yellow needles of **0** were grown by methanol/diethyl ether vapor diffusion of the compound at $25\text{ }^\circ\text{C}$. A crystal of dimensions $0.12 \times 0.12 \times 0.04$ mm was mounted on a Rigaku AFC10K Saturn 944+ CCD-based X-ray diffractometer equipped with a low temperature device and a Micromax-007HF Cu-target micro-focus rotating anode ($\lambda = 1.54187\text{ \AA}$) operated at 1.2 kW power (40 kV, 30 mA). The X-ray intensities were measured at 85(1) K with the detector placed at a distance of 42.00 mm from the crystal. A total of 2028 images were collected with an oscillation width of 1.0° in ω . The exposure times were 1 sec. for the low angle images, 8 sec. for high angle. Rigaku d*trek images were exported to CrysAlisPro⁵³ for processing and corrected for absorption. The integration of the data yielded a total of 181,810 reflections to a maximum 2θ value of 139.72° of which 22,253 were independent and 18,485 were greater than $2\sigma(I)$. The final cell constants (**Table S1**) were based on the xyz centroids of 40,190 reflections

above $10\sigma(I)$. Analysis of the data showed negligible decay during data collection. The structure was solved and refined with the Bruker SHELXTL (version 2018/3) software package,⁵⁴ using the space group P2/n with $Z = 4$ for the formula $2(C_{45}H_{59}N_8O_5Fe_2)$, $6(CF_3SO_3)$, $2.5(CH_3OH)$. All non-hydrogen atoms were refined anisotropically with the hydrogen atoms placed in a combination of refined and idealized positions. Two triflate anions and one bound methanol are disordered. Full matrix least-squares refinement based on F^2 converged at $R1 = 0.0859$ and $wR2 = 0.2388$ [based on $I > 2\sigma(I)$], $R1 = 0.0973$ and $wR2 = 0.2589$ for all data. Additional details are presented in **Tables S2-S7** and are given as Supporting Information in a CIF file, which was deposited in the CCDC (#2084746).

Yellow needles of **1** were grown by layering a dichloromethane/hexane solution of the compound at 25 °C. A crystal of dimensions 0.15 x 0.07 x 0.02 mm was mounted on a Rigaku AFC10K Saturn 944+ CCD-based X-ray diffractometer equipped with a low temperature device and a Micromax-007HF Cu-target micro-focus rotating anode ($\lambda = 1.54187 \text{ \AA}$) operated at 1.2 kW power (40 kV, 30 mA). The X-ray intensities were measured at 85(1) K with the detector placed at a distance of 42.00 mm from the crystal. A total of 2028 images were collected with an oscillation width of 1.0° in ω . The exposure times were 1 sec. for the low angle images, 8 sec. for high angle. Rigaku d*trek images were exported to CrysAlisPro⁵³ for processing and corrected for absorption. The integration of the data yielded a total of 44,463 reflections to a maximum 2σ value of 140.29° of which 10,747 were independent and 9361 were greater than $2\sigma(I)$. The final cell constants (**Table S8**) were based on the xyz centroids of 16,480 reflections above $10\sigma(I)$. Analysis of the data showed negligible decay during data collection. The structure was solved and refined with the Bruker SHELXTL (version 2018/3) software package,⁵⁴ using the space group P1bar with $Z = 2$ for the formula $C_{49}H_{58}N_8O_{11}F_6S_2Cl_4Fe_2$. All non-hydrogen atoms were refined anisotropically with the hydrogen atoms placed in a combination of refined and idealized positions. Full matrix least-squares refinement based on F^2 converged at $R1 = 0.0734$ and $wR2 = 0.2015$ [based on $I > 2\sigma(I)$], $R1 = 0.0808$ and $wR2 = 0.2131$ for all data. Additional details are presented in **Tables S9-S14** and are given as Supporting Information in a CIF file, which was deposited in the CCDC (#2084745).

DFT calculations. Geometry optimizations and frequency calculations were performed with Gaussian 09⁵⁵ and Gaussian 16⁵⁶ using the BP86 functional.⁵⁷ All calculations were performed with the 6-31G*⁵⁸⁻⁶¹ and then the TZVP^{62,63} basis set for geometry optimizations. Structures were

organized using three different fragments consisting of (1) the ligand backbone, (2) the first $\{\text{Fe}(\text{NO})_x\}^y$ unit, and (3) the second $\{\text{Fe}(\text{NO})_x\}^y$ unit. X-ray crystallographic structures were used as a starting point for the calculations. The structures of $\mathbf{0}(\text{NO})_2$, $\mathbf{1}(\text{NO})_2$, and $\mathbf{2}(\text{NO})_2$ were first fully optimized in the ferromagnetically-coupled state ($S_t = 3$) and then the spins were flipped to ultimately obtain the optimized structures of the molecules in the antiferromagnetically coupled ground state ($S_t = 0$).



Scheme 3. Preparation of the diferrous complexes **0**, **1**, and **2**, where the label represents the number of bridging acetate ligands.

3. Results and Analysis

3.1 Synthesis and spectroscopic characterization of **0**, **1**, and **2**.

The ligand N,N' -(6,6'-(((2-Hydroxy-5-methyl-1,3-phenylene)bis(methylene)bis((pyridin-2-ylmethyl)azanediyl))bis(methylene))bis(pyridine-6,2-diyl))bis(2,2-dimethylpropanamide) ($\text{H}[\text{BPMP}(\text{NHCO}^t\text{Bu})_2]$) was synthesized using published procedures^{50,51} and characterized by ^1H -NMR spectroscopy (**Scheme S1**). The complexes $[\text{Fe}_2(\text{BPMP}(\text{NHCO}^t\text{Bu})_2)(\text{OAc})_x](\text{OTf})_{3-x}$ (**0** – **2**, with $x = 0 - 2$ indicating the presence of 0, 1 or 2 acetate bridges) were obtained by metalation of the ligand $\text{H}[\text{BPMP}(\text{NHCO}^t\text{Bu})_2]$ with iron(II) triflate in the presence of the respective equivalents of sodium acetate (NaOAc). Complexes **0**, **1**, and **2** were dissolved in minimal

tetrahydrofuran (THF) and recrystallized from diethyl ether at -35 °C under air-free conditions to yield brown-orange crystalline solids. These precursor complexes were further characterized using UV-Vis and IR spectroscopy, and X-ray crystallography. In particular, IR spectroscopy provides information about the status of the amide groups in the second coordination sphere (SCS), and whether they are coordinated to the iron centers via their carbonyl O atoms as previously observed.^{50,64} As shown in **Figure 2**, the peak at 1700 cm⁻¹ for complex **2** is not present in the IR data of **0** and **1**. We assign this peak to the C=O stretch of the free amide groups, as further supported by the crystal structure of this compound that was previously reported (see **Figure 3**, right).⁵² The crystal structure of **2** shows that the amide groups are not coordinated to the iron centers, which is facilitated by the two acetate bridges occupying the open coordination sites of **2**. This value of the C=O stretch can be compared to the free ligand, where the amide C=O stretch is observed at 1687 cm⁻¹ by IR spectroscopy.⁵⁰

In contrast, for **0** and **1** coordination sites remain open to which the amide C=O moieties can coordinate, which decreases the C=O double bond character and shifts the corresponding stretching vibrations to distinctively lower energy. Attempts to identify the amide C=O stretching vibrations in **0** and **1** using ¹³C-labelled sodium acetate (CH₃¹³COONa) did not reveal new features, as the amide C=O stretches likely shift into the intense ligand bands in the lower energy region (**Figure S3**). Nevertheless, the identification of the free amide C=O moieties by IR spectroscopy provides a great handle to understand how amide coordination in the different model complexes changes under various conditions, including upon exposure to NO gas.

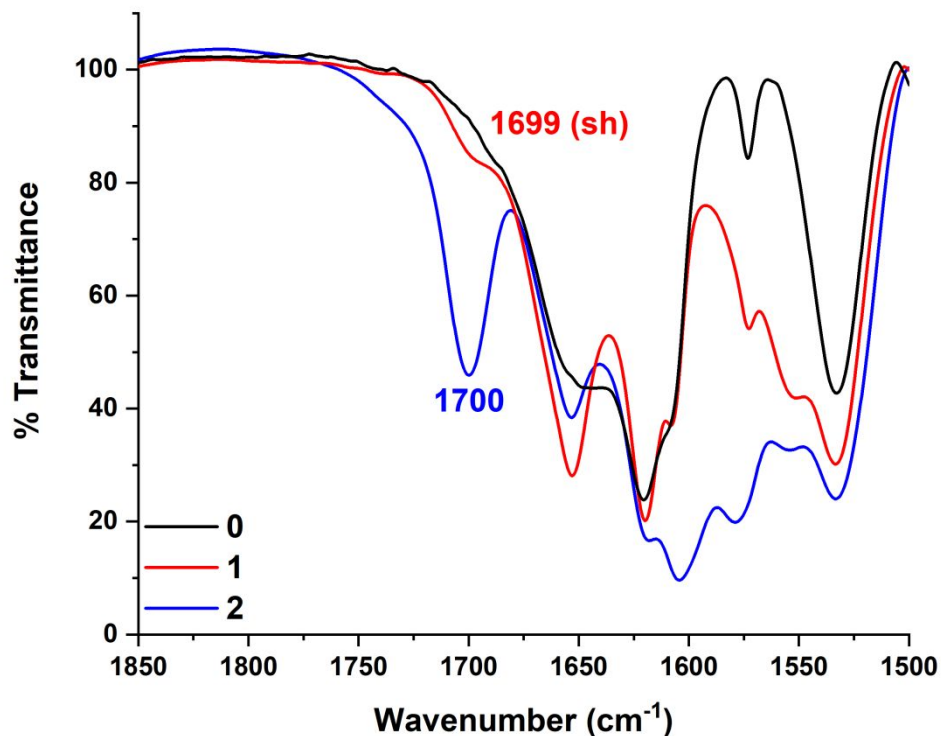


Figure 2. IR (KBr) spectra of the solid precursor complexes **0**, **1** and **2**.

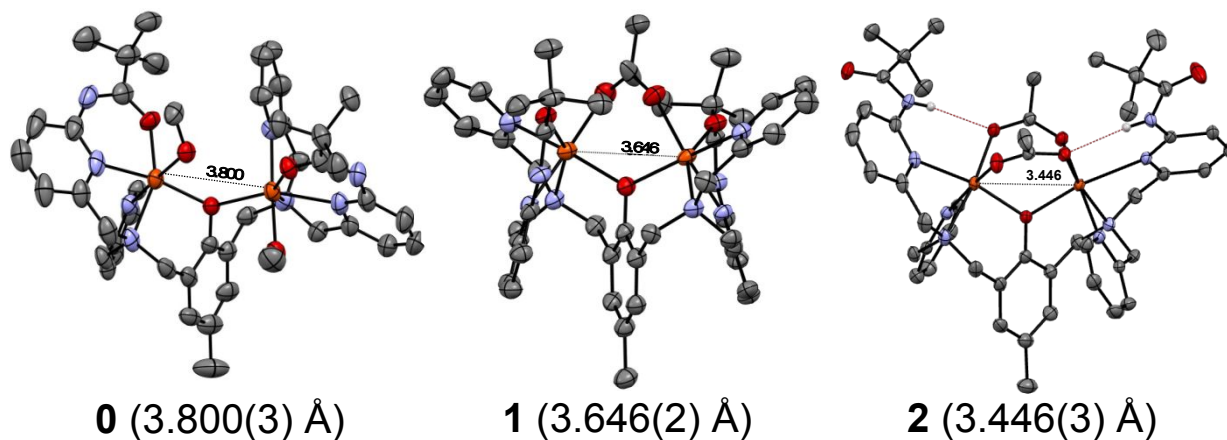


Figure 3. Crystal structures of **0** (CCDC #2084746), **1** (CCDC #2084745), and **2** (CCDC #1054874) with ellipsoids drawn at 50% probability. The OTf⁻ counter anions for **0** and **1** and the PF₆⁻ counter anion for **2**, solvent molecules, and hydrogen atoms (except for amide hydrogens in **2**) are omitted for clarity. The crystal structures show that hydrogen bonds are formed between the

bridging acetate ligands and the protons of the amide functional groups. The Fe-Fe distances in the different complexes are listed. The crystal structure of **2** was reported by Bernhardt et al.⁵²

The complex $[\text{Fe}_2(\text{BPMP}(\text{NHCO}^t\text{Bu})_2)(\text{OAc})_2](\text{PF}_6^-)$ (**2-PF₆**; the analog of **2** with a PF_6^- counter ion) was previously reported and structurally characterized by X-ray crystallography (**Figure 3**, right).⁵² The crystal structure for **2-PF₆** shows that the $\text{Fe}\cdots\text{Fe}$ distance is 3.45 Å. Importantly, the complex features N-H---O hydrogen bonds between the two outer-sphere amides and O atoms of the bridging acetate ligands as indicated in **Figure 3**. The hydrogen bond distances are about 2.2 Å, which corresponds to strong H-bonding interactions. In the case of the complex prepared with one equivalent of acetate, **1**, our crystallographic results indeed confirm a dimeric complex with a single bridging acetate ligand (**Figure 3**, middle). Interestingly, the pseudo-octahedral geometry of the iron centers is completed with the coordination of the O atoms of the amide groups. The $\text{Fe}\cdots\text{Fe}$ distance is 3.65 Å, which is elongated compared to complex **2-PF₆** (3.45 Å). The Fe-O(Ac) bond lengths are 2.10 and 2.09 Å, respectively (**Table 1**). The bridging acetate ligand is twisted to accommodate the coordination of the amides. The Fe-O(amide) bond lengths are 2.15 and 2.09 Å, respectively, showing that they are strongly coordinated to the iron centers. This result shows that there is no open coordination site for NO ligation in complex **1**. This is a problem that could lead to destabilization of the $[\text{hs}\{-\{\text{FeNO}\}^7\}]_2$ adduct. Further characterization of complex **1** with UV-vis spectroscopy shows a broad band at 393 nm (**Figure S14**). To complete the series, we decided to also include the complex without bridging acetate ligands, to evaluate how this affects the $\text{Fe}\cdots\text{Fe}$ distance and ultimately, the reactivity of the complexes with NO gas. Crystals of complex **0** were grown by slow diffusion of diethyl ether into a saturated solution of **0** in methanol. The crystal structure of **0** reveals again a dimeric structure with an $\text{Fe}\cdots\text{Fe}$ distance of 3.80 Å (**Figure 3**, left). The amide O atoms are again coordinated to the iron centers, with Fe-O(amide) bond lengths of 2.07 and 2.09 Å. The remaining, open coordination sites of the diiron core are occupied by MeOH solvent molecules, which complete the pseudo-octahedral geometry of the iron centers. Since solvent molecules like MeOH often bind weakly to transition metals, we believed that this complex could be fully nitrosylated when reacted with NO gas. Complex **0** shows a band at 381 nm in the UV-Vis spectrum (**Figure S13**).

In summary, when comparing the crystal structures of complexes **0** – **2**, a pattern emerges where the number of acetates bridges correlates with the $\text{Fe}\cdots\text{Fe}$ distances. Here, an increase in

the number of acetate bridges causes a distinct decrease in the Fe \cdots Fe distance, as shown in **Figure 3**. These distances are slightly longer than the reported Fe \cdots Fe distances in FNORs, which are observed between 3.2 and 3.4 Å for *Tm* FDP, for example.¹⁶ A shorter Fe \cdots Fe distance in the corresponding diiron dinitrosyl complexes would be expected to promote faster N–N coupling with a lower activation barrier, as the NO molecules are closer together.⁶⁵ At the same time, the acetate bridges and amide carbonyls occupy coordination sites in **1** and **2**, potentially preventing NO from binding to the complexes in the first place. In addition, amide coordination to the iron centers would prevent formation of the desired N–H \cdots ON hydrogen bonds (compare to **Scheme 2**). The reactions of complexes **0**–**2** with NO were therefore investigated in detail, to obtain insight into the factors affecting NO binding and activation.

Table 1. Comparison of structural parameters of the diferrous precursor complexes **0**–**2**.

Bonds	Diferrous precursor bond distances (Å)		
	0	1	2 ⁵²
Fe \cdots Fe	3.80(3)	3.64(2)	3.45(3)
Fe–O (bridging)*	2.08(3)	2.06(3)	2.06(1)
Fe–OAc*	N/A	2.09(3), 2.10(3)	2.10(1)
Fe–O (amide)	2.07(3), 2.09(3)	2.09(3), 2.15(3)	N/A
Fe–N (tertiary)*	2.22(4)	2.24(3)	2.23(2)
Fe–N (Pyr)*	2.20(4)	2.18(4)	2.25(2)
O \cdots H (H-bond)	N/A	N/A	2.21(3)

* = average value

3.2 Characterization of NO complexes **0**(NO)₂, **1**(NO)₂, and **2**(NO)₂

The nitrosylated complexes [Fe₂(BPMP(NHCO^tBu)₂)(NO)₂](OTf)₃ (**0**(NO)₂), [Fe₂(BPMP(NHCO^tBu)₂)(OAc)(NO)₂](OTf)₂ (**1**(NO)₂), and [Fe₂(BPMP(NHCO^tBu)₂)(μ-OAc)(NO)₂](OTf)₂ (**2**(NO)₂) were synthesized by reacting a solution of the corresponding diferrous precursor complex in CH₂Cl₂ with NO gas on the Schlenk line at 25 °C. The products were allowed

to stir for 1 hour before precipitation with hexanes overnight at $-35\text{ }^{\circ}\text{C}$. The resulting solids were collected over a frit using gravity filtration. $\mathbf{0}(\text{NO})_2$ was collected as a dark green solid. $\mathbf{1}(\text{NO})_2$ and $\mathbf{2}(\text{NO})_2$ were collected as dark brown-orange solids. The complexes were characterized using KBr IR (**Figure 4**), solution IR (**Figure 5**), and UV-vis spectroscopy (**Figure S17**).

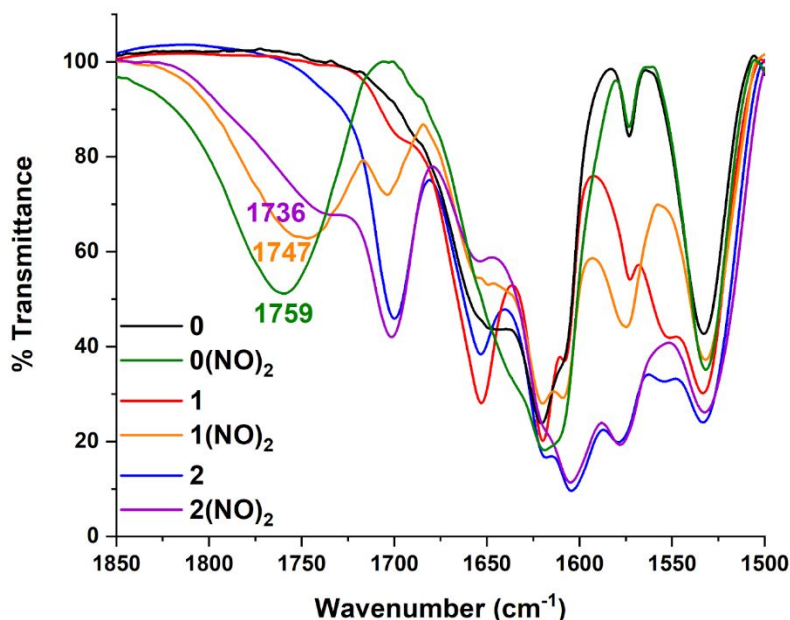


Figure 4. IR (KBr) spectra of the diferrous precursors **0**, **1**, and **2** and of the nitrosylated complexes $\mathbf{0}(\text{NO})_2$, $\mathbf{1}(\text{NO})_2$, and $\mathbf{2}(\text{NO})_2$.

As shown in **Figure 4**, the KBr IR spectra allow us to evaluate the coordination environments of the complexes in the solid state. For each of the NO complexes, a band is observed in the 1730–1760 cm^{-1} region, which corresponds to the N–O stretch in a $hs\text{-}\{\text{FeNO}\}^7$ complex.²⁵ Complex $\mathbf{0}(\text{NO})_2$ shows the most intense N–O stretching band at 1759 cm^{-1} , indicating strong NO binding, by displacement of the MeOH solvents from the iron centers (this complex does not contain any bridging acetate ligands). In addition, the IR spectrum shows no signal in the 1700 cm^{-1} region, indicating that the SCS amide O atoms are both coordinated to the iron centers, as shown in **Figure 6**. In comparison, the N–O stretch of $\mathbf{2}(\text{NO})_2$, observed at 1736 cm^{-1} , is merely a broad shoulder, indicating that the diferrous precursor **2** only has a weak affinity for NO. This is because the two iron centers in **2** are coordinatively saturated, in the presence of the two acetate bridges bound to the iron centers. In the NO adduct $\mathbf{2}(\text{NO})_2$, both SCS amide O atoms remain free (not coordinated to the iron centers), as indicated by the intense band at 1700 cm^{-1} , which is of equal intensity as

the same band in the precursor **2** (see **Figures 2** and **4**). Hence, upon NO binding, one of the bridging acetate ligands is replaced by NO in **2(NO)₂**, whereas the other acetate remains in a bridging coordination mode (denoted as μ -OAc). Complex **1(NO)₂** shows the N-O stretch at 1747 cm^{-1} with intermittent intensity. In the N-O complex, a band at 1700 cm^{-1} is further observed to rise upon NO coordination compared to **1**, with about half of the intensity as the corresponding signals in **2** and **2(NO)₂**. We take this as evidence that in **1(NO)₂**, one SCS amide O atom is no longer coordinated, whereas the other group remains bound, causing the two iron centers to have different primary coordination environments. This further implies that the acetate ligand switches to monodentate coordination upon NO binding to **1**. Based on this information, we propose the structures for the complexes **0(NO)₂**, **1(NO)₂**, and **2(NO)₂** shown in **Figure 6**.

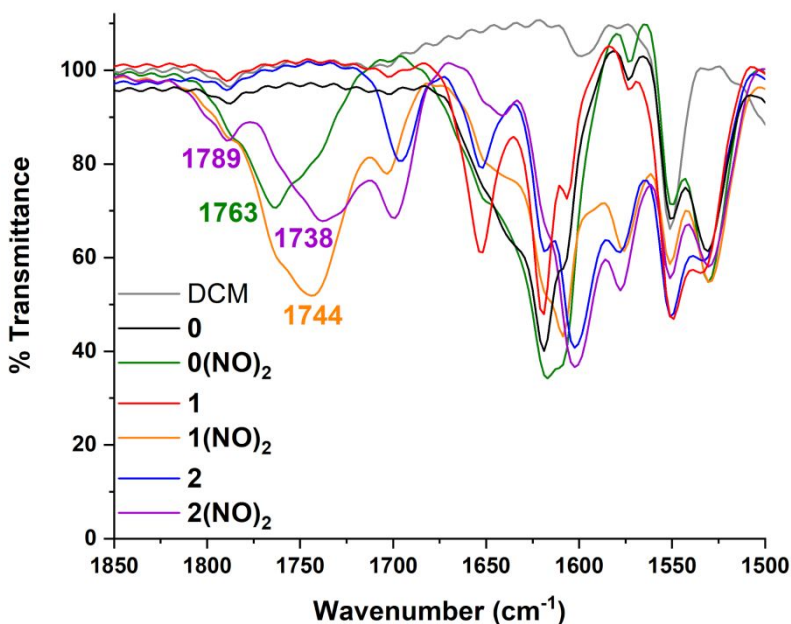


Figure 5. Solution IR spectra of the diferrous precursors **0**, **1**, and **2** and of the nitrosylated complexes **0(NO)₂**, **1(NO)₂**, and **2(NO)₂**, at a concentration of 10 mM in CH_2Cl_2 .

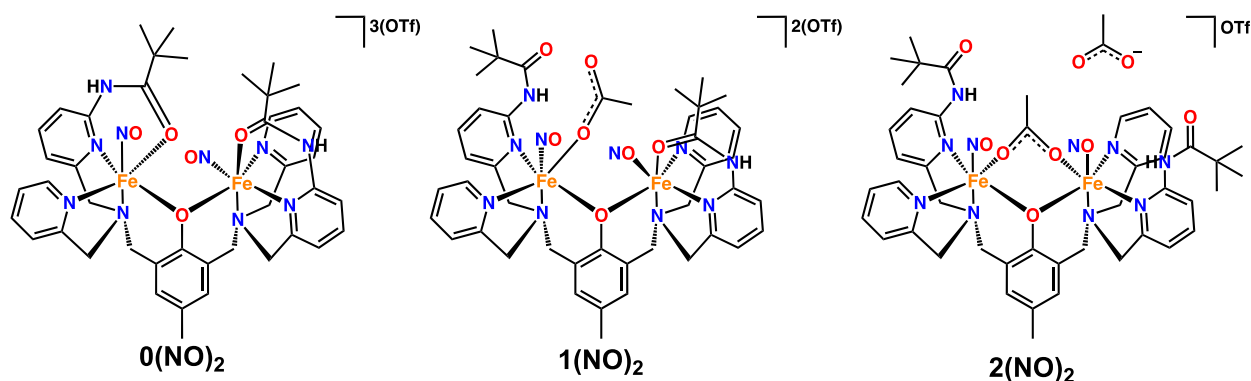


Figure 6. Proposed structures of $0(\text{NO})_2$, $1(\text{NO})_2$, and $2(\text{NO})_2$.

Similar effects can be observed in the solution IR spectra of the same complexes (**Figure 5**), which provides further insight into the solution state of the compounds. The N-O stretches of $0(\text{NO})_2$, $1(\text{NO})_2$, and $2(\text{NO})_2$ show slight shifts compared to the solid state, and are observed at 1763, 1744 and 1738 cm^{-1} , respectively, with the last complex also showing a second N-O stretching band at 1789 cm^{-1} of unknown origin. The trends in SCS amide O atom coordination are the same as observed in the solid state. Due to the presence of multiple NO complexes in solutions of $2(\text{NO})_2$, we focused our reactivity studies on $0(\text{NO})_2$ and $1(\text{NO})_2$, as described in Section 3.5.

3.3 Geometric structures of the NO complexes

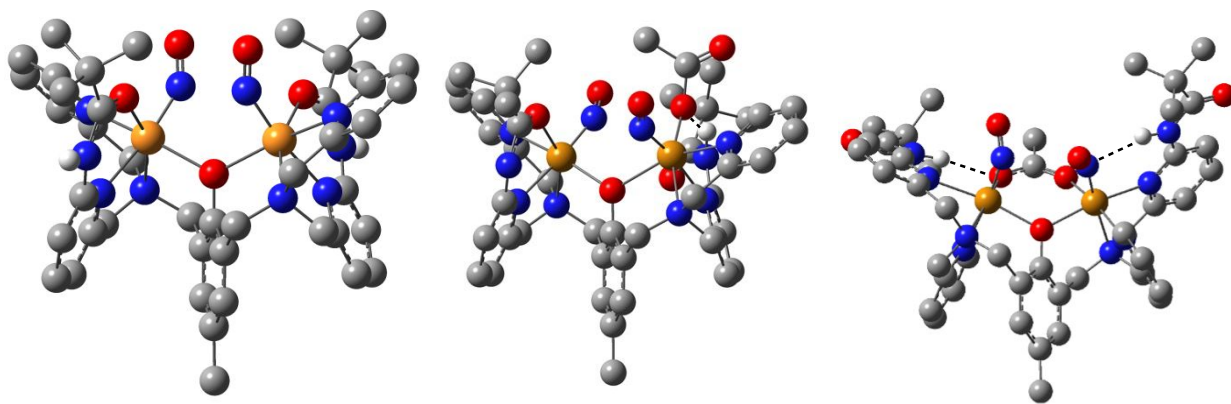


Figure 7. DFT-optimized structures of $0(\text{NO})_2$ (left), $1(\text{NO})_2$ (middle), and $2(\text{NO})_2$ (right) with hydrogen atoms (except for amide N-H groups) omitted for clarity. Hydrogen bonds are shown with dashed lines.

DFT-optimized molecular structures and frequencies were calculated for **0**(NO)₂, **1**(NO)₂, and **2**(NO)₂ as shown in **Figure 7**. The aim of this work was to supplement the crystallographic data of the precursor complexes by providing more detailed information on the structures of the nitrosylated complexes. The optimized structure of **0**(NO)₂ was found to closely match the structural features of both the precursor complex **0** and the mononitrosyl complex **1**(NO), reported in **Table 2**. The Fe-Fe distance in the optimized structure of **0**(NO)₂ is 3.87 Å, which is similar to the value obtained for the crystal structure of the precursor complex **0** (3.80 Å) and longer than that reported for the mononitrosyl complex, **1**(NO) (3.59 Å), due to the lack of a bridging acetate group.⁵⁰ The N-O distance in the optimized structure of **0**(NO)₂ is 1.17 Å, which is similar to the value reported for the mononitrosyl complex (1.16 Å).⁵⁰ Importantly, the (O)N-Fe-Fe-N(O) dihedral angle is predicted to be 63.4° in the optimized structure of **0**(NO)₂, which is similar to that in Fe₂(BPMP) complexes without a bridging acetate/propionate ligand: for example, in [Fe₂(BPMP)(OTf)₂(NO)₂](OTf), the (O)N-Fe-Fe-N(O) dihedral angle is 52.9°, obtained by X-ray crystallography.⁴⁹

The optimized structure of **1**(NO)₂ shows significant structural distortion compared to the experimental structures of **1**, **1**(NO),⁵⁰ and the DFT-optimized structure of **0**(NO)₂. This structural distortion is most prominent in the calculated Fe-O(bridging) distances of 2.10 Å and 2.36 Å (**Table 2**). Additionally, the structure has an elongated Fe-Fe distance of 3.90 Å. This Fe-Fe distance is similar to **0**(NO)₂ but significantly elongated compared to **1** and **1**(NO)⁵⁰ (**Table 2**). The structural distortion of **1**(NO)₂ is caused by the asymmetry introduced by the acetate unit binding in a monodentate fashion to one of the Fe centers and the carbonyl oxygen of the respective amide group binding to the other Fe center (determined by IR spectroscopy; see above). Interestingly, a strong hydrogen bonding interaction is observed by DFT between the coordinated oxygen of the acetate and the N-H group of the adjacent amide group, with a distance of 1.83 Å. This strong hydrogen bond likely stabilizes the monodentate binding mode of the acetate to one of the Fe centers. The N-O bond distances in **1**(NO)₂ are 1.17 and 1.18 Å, which matches well with those of the other nitrosyl complexes (**Table 2**). Significantly, the monodentate acetate sits between the two Fe-NO units causing a substantial (O)N-Fe-Fe-N(O) dihedral angle core distortion of 101.9°. We have previously shown that a small (O)N-Fe-Fe-N(O) dihedral angle is required for facile N-N coupling and N₂O formation in diiron complexes.⁴⁹ The major dihedral

distortion likely results in the lack of observable N₂O formation upon the addition of a chemical reductant to **1(NO)₂** (see below).

Unlike **1(NO)₂**, the optimized structure of **2(NO)₂** is similar to the experimental structures of complexes **0** and **1(NO)** (**Table 2**). The Fe-Fe distance in the optimized structure of **2(NO)₂** is 3.71 Å, which closely matches that of **1** and which is longer than that in the reported structure of **1(NO)**.⁵⁰ The N-O bond distances in **2(NO)₂** are 1.17 and 1.18 Å, which match well with those of **0(NO)₂** (1.17 Å) and **1(NO)** (1.16 Å). In contrast to the large (O)N-Fe-Fe-N(O) dihedral angles of **0(NO)₂** and **1(NO)₂**, **2(NO)₂** has a much smaller dihedral angle of 12.8°, which compares well with the (O)N-Fe-Fe-O(amide) dihedral angle of **1(NO)** (13.7°)⁵⁰ and that of the previously reported complex [Fe₂(BPMP)(OPr)(NO)₂](BPh₄)₂ (5.9°).⁴⁰

The N-O stretching frequencies were also calculated for **0(NO)₂**, **1(NO)₂**, and **2(NO)₂**. The calculated N-O frequencies for **0(NO)₂** are 1775 and 1749 cm⁻¹, with the 1775 cm⁻¹ mode being the main feature in the IR spectrum, which is in very good agreement with the experimental value of 1763 cm⁻¹ for **0(NO)₂**, shown in **Figure 5**. The calculated N-O vibrational frequencies for **1(NO)₂** are 1705 cm⁻¹ and 1756 cm⁻¹ with both modes having similar predicted intensities in the IR spectrum. This is in relatively good agreement with the experimental data with the broad IR feature at 1744 cm⁻¹ for **1(NO)₂** (**Figure 5**), likely accounting for the superposition of the two N-O vibrational stretching bands. Finally, the calculated N-O vibrational frequencies for **2(NO)₂** are 1743 cm⁻¹ and 1690 cm⁻¹, with the 1743 cm⁻¹ mode being the major contributing feature in the IR spectrum. This is in very good agreement with the experimental value of 1738 cm⁻¹ for **2(NO)₂**, shown in **Figure 5**.

Table 2. Comparison of structural parameters of the complexes **0**, **1**, **1(NO)**, and the DFT-optimized NO complexes.

Bonds	0	1	1(NO) ⁵⁰	0(NO)₂ DFT	1(NO)₂ DFT	2(NO)₂ DFT
Fe···Fe (Å)	3.80(3)	3.65(2)	3.59(1)	3.87	3.90	3.71
Fe-O (Bridging) (Å)	2.08(3)*	2.06(3)*	2.06(3)*	2.16*	2.10, 2.36	2.13*
Fe-OAc (Å)	N/A	2.10(3)*	2.07(3)*	N/A	1.95	2.08*

Fe-O (Amide) (Å)	2.07(3), 2.09(3)	2.09(3), 2.15(3)	2.06(3)	2.10, 2.10	2.14	N/A
Fe-N (tertiary)* (Å)	2.22(4)	2.24(3)	2.20(4)	2.24	2.23	2.22
Fe-N (Pyr)* (Å)	2.20(4)	2.18(4)	2.19(4)	2.19	2.22	2.23
Fe-NO (Å)	N/A	N/A	1.82(4)	1.76	1.75, 1.74	1.76, 1.75
N-O (Å)	N/A	N/A	1.16(6)	1.17	1.17, 1.18	1.17, 1.18
AcO \cdots HN (Å) (H-bond)	N/A	N/A	2.10	N/A	1.83	2.16
ON \cdots HN (Å) (H-bond)	N/A	N/A	N/A	N/A	N/A	2.24
Fe-N-O angle (°)	N/A	N/A	N/A	145.92*	149.40, 148.44	146.41, 144.81
(ON)-Fe-Fe-(NO) dihedral angle (°)	N/A	N/A	N/A	61.57	101.91	12.79

* = average value

3.4 Reactivity of NO complexes **0**(NO)₂ and **1**(NO)₂

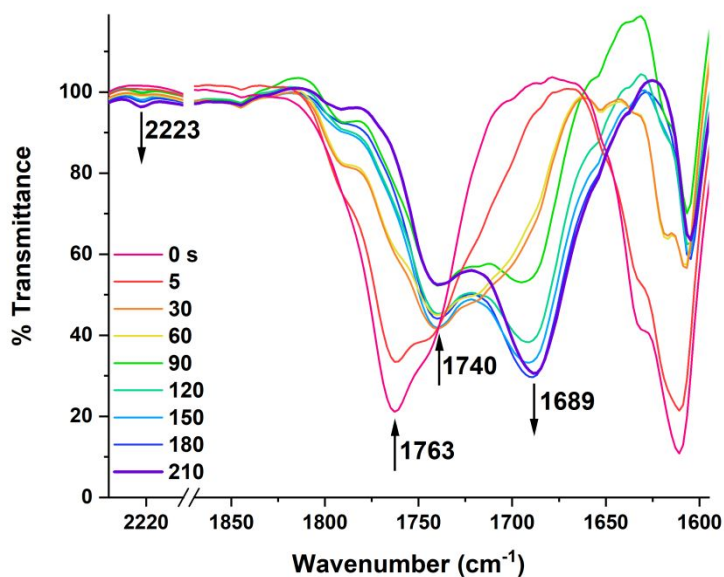


Figure 8. IR-spectroelectrochemical data of **0**(NO)₂ with the potential held at -1.4 V vs. Ag wire. Conditions were 10 mM in CH₂Cl₂ with 0.1 M [TBA](OTf) as the supporting electrolyte.

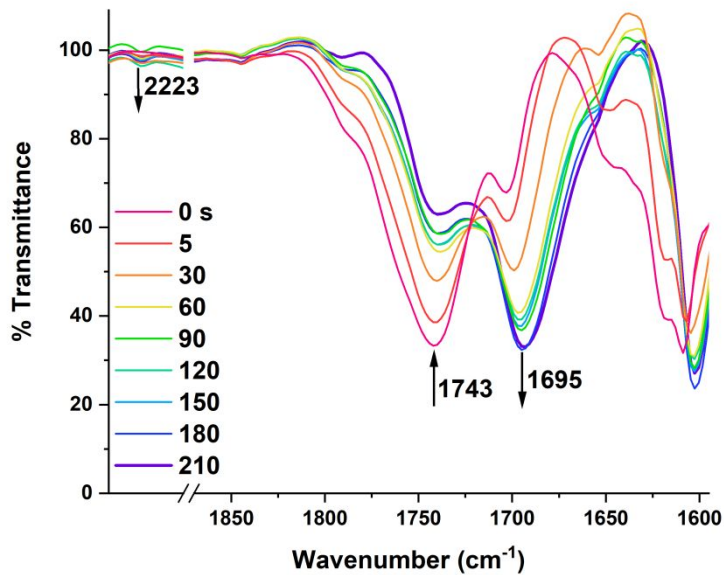


Figure 9. IR-spectroelectrochemical data of **1**(NO)₂ with the potential held at -1.4 V vs. Ag wire. Conditions were 10 mM in CH₂Cl₂ with 0.1 M [TBA](OTf) as the supporting electrolyte.

Since the NO complexes **0**(NO)₂ and **1**(NO)₂ are stable in solution and do not mediate N-N coupling and N₂O formation, we further investigated whether N₂O formation could be enabled by one-electron reduction of the complexes, following the semireduced mechanism.^{34,35,37} These investigations were conducted using IR-spectroelectrochemistry (SEC-IR). Here, IR spectra are recorded in a thin layer solution cell under an applied, constant potential. For the **0**(NO)₂ complex, applying a potential of -1.4 V vs. Ag wire led to the disappearance of the N-O stretch at 1763 cm⁻¹ and the appearance of two peaks at 1740 and 1689 cm⁻¹, as shown in **Figure 8**. Similar reactivity was observed for the complex **1**(NO)₂, shown in **Figure 9**, where, upon reduction, the N-O stretching band at 1743 cm⁻¹ disappeared. After 210 seconds, two new peaks were observed at 1740 and 1695 cm⁻¹, similar to the product resulting from reduction of **0**(NO)₂. This intense two-peak pattern observed in the SEC-IR spectra of both **0**(NO)₂ and **1**(NO)₂ is characteristic for the formation of dinitrosyl iron complexes (DNICs) in solution as the main reaction products.^{25,49,66-68} To better understand the identity of the peaks, **0** was reacted with ¹⁵NO to generate **0**(¹⁵NO)₂. The resulting complex was investigated using SEC-IR under the same conditions (**Figure S11**). A shift in the N-O stretch was observed, from 1763 cm⁻¹ to 1732 cm⁻¹, in the dinitrosyl complex, but due to the rather low degree of nitrosylation of this complex, the shifted DNIC peaks are difficult to identify, as they overlap with other intense IR signals. However, from the data it is clear that the DNIC signals at 1740 and 1689 cm⁻¹ are ¹⁵NO-isotope sensitive, which further confirms our assignments.

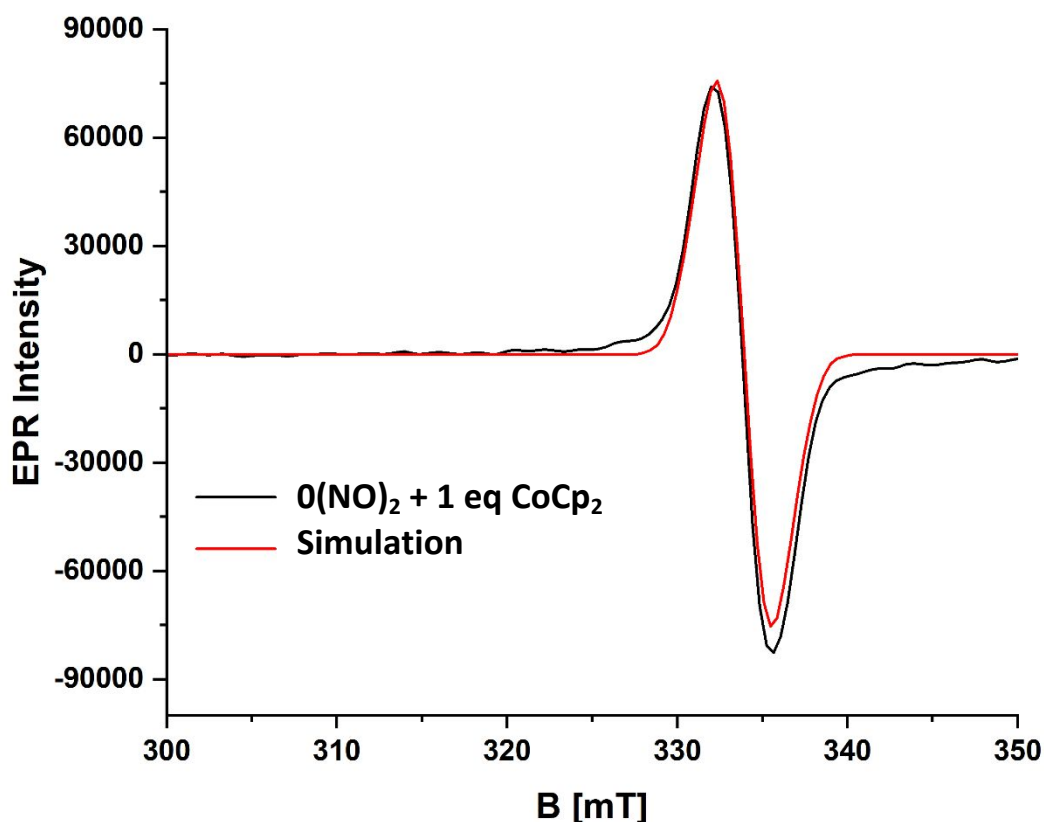


Figure 10. EPR spectrum and fit for the DNIC resulting from the reduction of $\mathbf{0}(\text{NO})_2$ with 1 equivalent of CoCp_2 in dichloromethane. Sample concentration was 3 mM. The $S = 1/2$ data were simulated with $g_x = g_y = 2.008$, $g_z = 2.000$ and $sg_x = sg_y = sg_z = 0.01$. The program SpinCount by Prof. M. P. Hendrich (Carnegie Mellon University) was used for the simulation.

The observed vibrational energies for the DNICs at about 1740 and 1690 cm^{-1} are in between those reported previously for the $\{\text{Fe}(\text{NO})_2\}^9$ and $\{\text{Fe}(\text{NO})_2\}^{10}$ complexes obtained for the related $\text{Fe}_2(\text{BPMP})$ platform by White and Lengel et al.⁴⁹ We therefore conducted EPR measurements to determine the nature of the DNIC product formed in the reduction of $\mathbf{0}(\text{NO})_2$. These results, shown in **Figure 10**, identify the product as an $S_t = 1/2$ $\{\text{Fe}(\text{NO})_2\}^9$ complex. A simulation of these data further confirms this assignment.

Quantitative N_2O yield experiments were performed to determine if any N_2O is formed upon reduction of $\mathbf{0}(\text{NO})_2$ and $\mathbf{1}(\text{NO})_2$. For this purpose, the NO complexes were reduced with 1 equivalent of cobaltocene (CoCp_2) in sealed flasks, and then the gas headspace of the flasks was

analyzed by IR spectroscopy. No N_2O was detected after both 5 minutes and 2 hours in these experiments, indicating that DNICs are the sole products of the one-electron reduction of $\mathbf{0}(\text{NO})_2$ and $\mathbf{1}(\text{NO})_2$. To further interrogate the nature of the reaction products, we attempted to precipitate and isolate the DNIC resulting from the 5-minute reduction of $\mathbf{0}(\text{NO})_2$ with CoCp_2 . The KBr IR spectrum of the resulting solid is shown in **Figure S4**, but no signals corresponding to new products could be observed in these experiments.

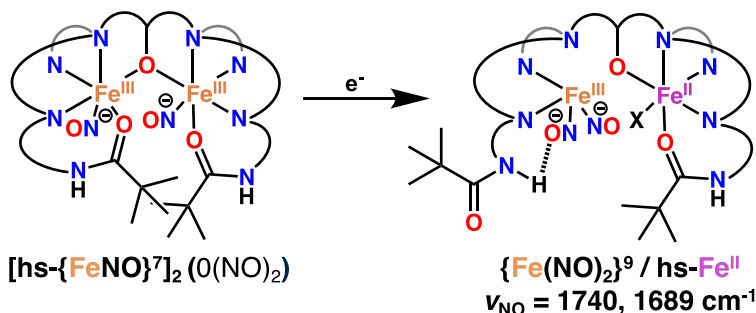
4. Discussion

In this work, a H[BPMP] ligand derivative with amide groups in the second coordination sphere (SCS) has been prepared to explore the effects of hydrogen-bonding on the electronic structure and reactivity of diiron dinitrosyl complexes that model Flavodiiron NO Reductases (FNORs). Three related compounds with 0 - 2 acetate bridges have been prepared and fully characterized. The crystal structures of these precursor complexes show an interesting relation between the $\text{Fe}\cdots\text{Fe}$ distance and the number of bridging acetates; here, the $\text{Fe}\cdots\text{Fe}$ distance decreases when the number of bridging acetates increases. The corresponding diiron dinitrosyl complexes were then prepared for all three compounds and fully characterized. Unfortunately, in the given ligand scaffold, the O atoms of the amide groups compete with NO for binding to the iron centers. It was further found that the N-H groups of the SCS amide groups do not hydrogen bond to the coordinated NO ligands. Instead, the C=O groups of the amides rotate and coordinate to the iron centers. Computational studies using DFT support this result, as observed in the fully optimized structures of $\mathbf{0}(\text{NO})_2$ and $\mathbf{1}(\text{NO})_2$. Additionally, complex **2** has a very low affinity for NO, preventing full formation of a diiron dinitrosyl species. The N-O stretching frequencies of these complexes were found to be $>1700\text{ cm}^{-1}$, indicating that the complexes are unable to perform direct NO reduction.^{25,45} However, we were still interested in understanding how the structures of these complexes, due to the SCS interactions, affect their ability to mediate NO reduction via the semireduced pathway (see Scheme 1). Upon one-electron reduction, complexes $\mathbf{0}(\text{NO})_2$ and $\mathbf{1}(\text{NO})_2$ do not generate any N_2O , but instead, show formation of Dinitrosyl Iron Complexes (DNICs). Further experimental results, including solution IR and EPR data, support the formation of DNICs from complexes $\mathbf{0}(\text{NO})_2$ and $\mathbf{1}(\text{NO})_2$ upon reduction.

Based on our EPR data, the DNICs observed in our reactivity studies are of $\{\text{Fe}(\text{NO})_2\}^9$ type and show an $S_t = 1/2$ ground state. Reducing both $\mathbf{0}(\text{NO})_2$ and $\mathbf{1}(\text{NO})_2$ led to the formation of similar DNICs, as evident from their very similar vibrational properties, with N-O stretching frequencies of about 1740 and 1690 cm^{-1} . The splitting between the two N-O stretching bands, $\Delta\nu(\text{N-O})$, in the $\{\text{Fe}(\text{NO})_2\}^9$ DNICs is about 50 cm^{-1} . Based on literature comparisons, this is also in agreement with the formation of $\{\text{Fe}(\text{NO})_2\}^9$ DNICs.^{49,69-71} Here, four-coordinate (4C) DNICs are reported to have $\Delta\nu(\text{N-O})$ values between 45 and 70 cm^{-1} , indicating that the DNICs formed from $\mathbf{0}(\text{NO})_2$ and $\mathbf{1}(\text{NO})_2$ have 4C structures as well.⁴⁹ Based on this information, we propose the structures shown in **Scheme 4** for the observed $\{\text{Fe}(\text{NO})_2\}^9/\text{hs-Fe}^{\text{II}}$ DNIC and putative $\{\text{Fe}(\text{NO})_2\}^{10}/\text{hs-Fe}^{\text{II}}$ DNIC resulting from reduction of $\mathbf{0}(\text{NO})_2$. The DNIC product could potentially be stabilized by hydrogen bonding between an NO molecule and the SCS amide groups. Additionally, the lower energy N-O stretch of the DNIC around 1690 cm^{-1} may overlap with the C=O stretch of the free amide SCS groups at about 1700 cm^{-1} . Further work is necessary to differentiate these two features.

These observations agree with experimental data from previous work from our group. White and Lengel et al. previously identified that the (O)N-Fe-Fe-N(O) dihedral angle in $[\text{Fe}_2(\text{BPMP})(\mathbf{X})_{(n)}(\text{NO})_2]^{3+/2+/+}$ type complexes plays a crucial role in determining the reactivity of the complexes upon one-electron reduction (semireduction).⁴⁹ In the presence of a **bridging** acetate/propionate (= \mathbf{X} , $n = 1$), the two [FeNO] units are coplanar, with an (O)N-Fe-Fe-N(O) dihedral angle of only 5.9°, leading to quantitative N_2O formation and no DNICs are observed. However, when monodentate ligands are used for \mathbf{X} ($n = 2$), for example triflate ($\mathbf{X} = \text{OTf}^-$), the (O)N-Fe-Fe-N(O) dihedral angle for the corresponding complex is 52.9°, leading to retarded N_2O yields below 10% and DNICs are formed as the major products. Detailed investigations have further shown that the DNICs are bimolecular, with the DNIC tethered to a non-heme iron center as indicated in **Scheme 4**. The results reported in this paper parallel those studies: our DFT-optimized structure for $\mathbf{0}(\text{NO})_2$ shows a very similar dihedral (O)N-Fe-Fe-N(O) angle of 63.4°, likely due to distortion from the amide C=O groups coordinated to the iron centers, and accordingly, complexes $\mathbf{0}(\text{NO})_2$ and $\mathbf{1}(\text{NO})_2$ do not show N_2O formation upon reduction. Interestingly, the calculated structure of $\mathbf{1}(\text{NO})_2$ reveals a dihedral angle of 101.9° due to the formation of a monodentate (instead of bridging) acetate ligand, which further distorts the core

and inhibits the N-N coupling pathway. This reveals the importance of the acetate group and the requirement for the bidentate binding mode to facilitate N-N coupling and N₂O formation.



Scheme 4. Formation of a $\{\text{Fe}(\text{NO})_2\}^9$ DNIC complex from $\mathbf{0}(\text{NO})_2$.

There are also some key differences between the DNICs formed here and those observed in the $[\text{Fe}_2(\text{BPMP})(\text{X})_{(n)}(\text{NO})_2]^{3+/+}$ system. The $\{\text{Fe}(\text{NO})_2\}^9/\text{hs}\text{-Fe}^{\text{II}}$ DNICs obtained from the $[\text{Fe}_2(\text{BPMP})(\text{X})_{(n)}(\text{NO})_2]^{3+/+}$ type complexes with monodentate ligands **X** show N-O stretching frequencies of 1788 and 1715 cm^{-1} , which is significantly different from those observed here, at about 1740 and 1690 cm^{-1} . In addition, whereas the DNICs from the $\text{Fe}_2(\text{BPMP})$ ligand platform are able to form N₂O over the course of 2 hours (depending on the conditions), the DNICs obtained here with the $\text{Fe}_2(\text{BPMP}(\text{NHCO}^t\text{Bu})_2)$ platform are stable, and unable to generate N₂O over time. We attribute these key differences to the presence of hydrogen bonds between the NO ligands of the DNIC and the SCS amide groups in the $\text{Fe}_2(\text{BPMP}(\text{NHCO}^t\text{Bu})_2)$ case, which stabilize the DNICs and cause a change in the electronic structure, responsible for the shift in the N-O stretching frequencies. This is further supported by a recent report by Layfield and coworkers: here, it was observed that upon binding of a strong Lewis acid to the NO ligands in a DNIC, a large shift of the N-O stretching frequencies to lower wavenumbers was observed.⁷² These results demonstrate again how hydrogen-bonding, as a key SCS interaction in proteins, is able to alter the reactivity of transition-metal complexes.

The amide-appended ligands were initially designed to promote hydrogen-bonding between the coordinated NO molecules and the amide N-H groups in the $[\text{hs}\{-\text{FeNO}\}^7]_2$ intermediates, but this was not actually observed here, due to the ability of the O atoms of the amide groups to coordinate to the iron centers, instead of forming such hydrogen bonds. This suggests that the amide groups may not be positioned optimally for hydrogen-bonding with the NO ligands. Further

work is necessary to explore alternative ligand designs for stabilizing a Fe-NO structure with strong hydrogen bonds.

5. Conclusion

In this work, we present a study on the role of second coordination sphere (SCS) groups on the reduction of nitric oxide (NO) to N₂O by diiron FNOR model complexes. We chose an amide-appended ligand scaffold to investigate its ability to hydrogen bond to the Fe-NO groups. We also varied the number of acetate bridges between the iron centers to probe how this affects the Fe-Fe distance of the complexes, finding that increasing the number of bridges decreases the distance between the iron centers. This feature could influence the kinetics of N-N bond formation to produce N₂O. Upon one-electron reduction, these complexes were found to produce Dinitrosyl Iron Complexes (DNICs), instead of producing N₂O. These results provide new insights into the general reactivity of non-heme diiron complexes with NO, and how NO activation is influenced by the SCS. Future work in this area includes the application of different hydrogen bond donors in the H[BPMP] ligand backbone, to allow for H-bond formation without affecting the coordination environment of the iron centers.

ASSOCIATED CONTENT:**Supporting Information:**

The Supporting Information is available free of charge at _____ and contains information on the following: additional UV-Vis, FT-IR, CV, NMR, X-ray crystallography data and DFT-optimized coordinates. Supplementary crystallographic data can be found at CCDC deposition #2084745 and #2084746 and can be obtained free of charge.

AUTHOR INFORMATION:**Corresponding Author**

*E-mail: lehnertn@umich.edu

ORCID:

Nicolai Lehnert: 0000-0002-5221-5498

Abigail J. Bracken: 0000-0003-0988-1118

Hai T. Dong: 0000-0002-8914-3045

Michael O. Lengel: 0000-0002-1003-4357

Funding Sources:

National Science Foundation

Conflicts of Interest:

There are no conflicts to declare.

ACKNOWLEDGMENT:

This work was supported by the National Science Foundation (CHE-2002885 to NL). We acknowledge Dr. Jeff Kampf (University of Michigan) for X-ray crystallographic analysis of **0** and **1** and funding from NSF grant CHE-0840456 for X-ray instrumentation.

References

1. Furchgott, R. F. Endothelium-Derived Relaxing Factor: Discovery, Early Studies, and Identification as Nitric Oxide (Nobel Lecture). *Angew. Chem. Int. Ed.* **1999**, *38*, 1870-1880.
2. Ignarro, L. Nitric Oxide: A Unique Endogenous Signaling Molecule in Vascular Biology (Nobel Lecture). *Angew. Chem. Int. Ed.* **1999**, *38*, 1882-1892.
3. Murad, F. Discovery of Some of the Biological Effects of Nitric Oxide and Its Role in Cell Signaling (Nobel Lecture). *Angew. Chem. Int. Ed.* **1999**, *38*, 1856-1868.
4. Lehnert, N.; Berto, T. C.; Galinato, M. G. I.; Goodrich, L. E. In *The Role of Heme-Nitrosyls in the Biosynthesis, Transport, Sensing, and Detoxification of Nitric Oxide (NO) in Biological Systems: Enzymes and Model Complexes*; Kadish, K. M., Smith, K. M., Guillard, R., Eds.; World Scientific: New Jersey, 2011; Vol. 14,, p 1-247
5. Ignarro, L. *Nitric Oxide: Biology and Pathobiology*; Academic Press: San Diego, 2000.
6. Wink, D. A.; Mitchell, J. B. Chemical biology of nitric oxide: insights into regulatory, cytotoxic, and cytoprotective mechanisms of nitric oxide. *Free Rad. Biol. Med.* **1998**, *25*, 434-456.
7. Stuehr, D. J.; Gross, S. S.; Sakuma, I.; Levi, R.; Nathan, C. F. Activated Murine Macrophages Secrete a Metabolite of Arginine with the Bioactivity of Endothelium-Derived Relaxing Factor and the Chemical Reactivity of Nitric Oxide. *J. Exp. Med.* **1989**, *169*, 1011-1020.
8. Gardner, P. R.; Martin, L. A.; Hall, D.; Gardner, A. M. Dioxygen-dependent metabolism of nitric oxide in mammalian cells. *Free Rad. Biol. Med.* **2001**, *31*, 191-204.
9. Møller, J. K. S.; Skibsted, L. H. Nitric Oxide and Myoglobins. *Chem. Rev.* **2002**, *102*, 1167-1178.
10. White, C. J.; Lehnert, N.; Meyerhoff, M. E. Electrochemical generation of nitric oxide for medical applications. *Electrochem. Sci. Adv.* **2022**, *2*, e2100156.
11. Caranto, J. D.; Weitz, A.; Giri, N.; Hendrich, M. P.; Kurtz, D. M. A Diferrous-Dinitrosyl Intermediate in the N₂O-Generating Pathway of a De flavinated Flavo-Diiron Protein. *Biochemistry* **2014**, *53*, 5631-5637.
12. Gardner, A. M.; Gessner, C. R.; Gardner, P. R. Regulation of the Nitric Oxide Reduction Operon (*norRVW*) in *Escherichia coli*. Role of NorR and σ^{54} in the Nitric Oxide Stress Response. *J. Biol. Chem.* **2003**, *278*, 10081-10086.
13. Missall, T. A.; Lodge, J. K.; McEwen, J. E. Mechanisms of Resistance to Oxidative and Nitrosative Stress: Implications for Fungal Survival in Mammalian Hosts. *Eucaryot. Cell* **2004**, *3*, 835-846.
14. Sarti, P.; Fiori, P. L.; Forte, E.; Rappelli, P.; Teixeira, M.; Mastronicola, D.; Sancier, G.; Giuffr , A.; Brunori, M. *Trichomonas vaginalis* degrades nitric oxide and expresses a flavorubredoxin-like protein: a new pathogenic mechanism? *Cell. Mol. Life Sci.* **2004**, *61*, 618-623.
15. Fraz o, C.; Silva, G.; Gomes, C. M.; Matias, P.; Coelho, R.; Sieker, L.; Macedo, S.; Liu, M. Y.; Oliveira, S.; Teixeira, M.; Xavier, A. V.; Rodrigues-Pousada, C.; Carrondo, M. A.; Le Gall, J. Structure of a dioxygen reduction enzyme from *Desulfovibrio gigas*. *Nat. Struct. Biol.* **2000**, *7*, 1041-1045.
16. Silaghi-Dumitrescu, R.; Kurtz, D. M., Jr.; Ljungdahl, L. G.; Lanzilotta, W. N. X-ray Crystal Structures of *Moorella thermoacetica* FprA. Novel Diiron Site Structure and Mechanistic Insights into a Scavenging Nitric Oxide Reductase. *Biochemistry* **2005**, *44*, 6492-6501.

17. Mills, P. C.; Rowley, G.; Spiro, S.; Hinton, J. C. D.; Richardson, D. J. A combination of cytochrome c nitrite reductase (NrfA) and flavorubredoxin (NorV) protects *Salmonella enterica* serovar Typhimurium against killing by NO in anoxic environments. *Microbiol.-Sgm* **2008**, *154*, 1218-1228.
18. Gomes, C. M.; Giuffrè, A.; Forte, E.; Vicente, J. B.; Saraiva, L. M.; Brunori, M.; Teixeira, M. A Novel Type of Nitric-oxide Reductase. *Escherichia Coli* Flavorubredoxin. *J. Biol. Chem.* **2002**, *277*, 25273-25276.
19. Anstey, N. M.; Weinberg, J. B.; Hassanali, M. Y.; Mwaikambo, E. D.; Manyenga, D.; Misukonis, M. A.; Arnelle, D. R.; Hollis, D.; McDonald, M. I.; Granger, D. L. Nitric oxide in Tanzanian children with malaria: inverse relationship between malaria severity and nitric oxide production/nitric oxide synthase type 2 expression. *J. Exp. Med.* **1996**, *184*, 557-567.
20. Evans, T. G.; Thai, L.; Granger, D. L.; Hibbs, J. B., Jr Effect of in vivo inhibition of nitric oxide production in murine leishmaniasis. *J. Immunol.* **1993**, *151*, 907-915.
21. Stenger, S.; Donhauser, N.; Thüring, H.; Röllinghoff, M.; Bogdan, C. Reactivation of latent leishmaniasis by inhibition of inducible nitric oxide synthase. *J. Exp. Med.* **1996**, *183*, 1501-1514.
22. Nicholson, S.; Bonecini-Almeida, M. d. G.; Lapa e Silva, J. R.; Nathan, C.; Xie, Q. W.; Mumford, R.; Weidner, J. R.; Calaycay, J.; Geng, J.; Boechat, N.; Linhares, C.; Rom, W.; Ho, J. L. Inducible nitric oxide synthase in pulmonary alveolar macrophages from patients with tuberculosis. *J. Exp. Med.* **1996**, *183*, 2293-2302.
23. Privett, B. J.; Broadnax, A. D.; Bauman, S. J.; Riccio, D. A.; Schoenfisch, M. H. Examination of bacterial resistance to exogenous nitric oxide. *Nitric Oxide* **2012**, *26*, 169-173.
24. Kurtz, D. M., Jr. Flavo-Diiron Enzymes: Nitric Oxide or Dioxygen Reductases? *Dalton Trans.* **2007**, 4115-4121.
25. Lehnert, N.; Kim, E.; Dong, H. T.; Harland, J. B.; Hunt, A. P.; Manickas, E. C.; Oakley, K. M.; Pham, J.; Reed, G. C.; Sosa Alfaro, V. The Biologically Relevant Coordination Chemistry of Iron and Nitric Oxide: Electronic Structure and Reactivity. *Chem. Rev.* **2021**, *121*, 14682-14905.
26. Romão, C. V.; Vicente, J. B.; Borges, P. T.; Frazão, C.; Teixeira, M. The Dual Function of Flavodiiron Proteins: Oxygen and/or Nitric Oxide Reductases. *J. Bio. Inorg. Chem.* **2016**, *21*, 39-52.
27. Biswas, S.; Kurtz, D. M.; Montoya, S. R.; Hendrich, M. P.; Bominaar, E. L. The Catalytic Role of a Conserved Tyrosine in Nitric Oxide-Reducing Non-heme Diiron Enzymes. *ACS Catal.* **2020**, *10*, 8177-8186.
28. Caranto, J. D.; Weitz, A.; Giri, N.; Hendrich, M. P.; Kurtz, D. M., Jr. A Diferrous-Dinitrosyl Intermediate in the N₂O-Generating Pathway of a Deflavinated Flavo-Diiron Protein. *Biochemistry* **2014**, *53*, 5631-5637.
29. Caranto, J. D.; Weitz, A.; Hendrich, M. P.; Kurtz, D. M., Jr. The Nitric Oxide Reductase Mechanism of a Flavo-Diiron Protein: Identification of Active-Site Intermediates and Products. *J. Am. Chem. Soc.* **2014**, *136*, 7981-7992.
30. Enemark, J. H.; Feltham, R. D. Principles of Structure, Bonding, and Reactivity for Metal Nitrosyl Complexes. *Coord. Chem. Rev.* **1974**, *13*, 339-406.
31. Brown, C. A.; Pavlosky, M. A.; Westre, T. E.; Zhang, Y.; Hedman, B.; Hodgson, K. O.; Solomon, E. I. Spectroscopic and Theoretical Description of the Electronic Structure of S = 3/2 Iron-Nitrosyl Complexes and Their Relation to O₂ Activation by Non-Heme Iron Enzyme Active Sites. *J. Am. Chem. Soc.* **1995**, *117*, 715-732.

32. Berto, T. C.; Hoffman, M. B.; Murata, Y.; Landenberger, K. B.; Alp, E. E.; Zhao, J.; Lehnert, N. Structural and Electronic Characterization of Non-Heme Fe(II)-Nitrosyls as Biomimetic Models of the Fe_B Center of Bacterial Nitric Oxide Reductase (NorBC). *J. Am. Chem. Soc.* **2011**, *133*, 16714–16717.
33. Berto, T. C.; Speelman, A.; Zheng, S.; Lehnert, N. Mono- and Dinuclear Non-Heme Iron-Nitrosyl Complexes: Models for Key Intermediates in Bacterial Nitric Oxide Reductases. *Coord. Chem. Rev.* **2013**, *257*, 244-259.
34. White, C. J.; Speelman, A. L.; Kupper, C.; Demeshko, S.; Meyer, F.; Shanahan, J. P.; Alp, E. E.; Hu, M.; Zhao, J.; Lehnert, N. The Semireduced Mechanism for Nitric Oxide Reduction by Non-Heme Diiron Complexes: Modeling Flavodiiron Nitric Oxide Reductases. *J. Am. Chem. Soc.* **2018**, *140*, 2562-2574.
35. Jana, M.; White, C. J.; Pal, N.; Demeshko, S.; Meyer, F.; Lehnert, N.; Majumdar, A. Functional Models for the Mono- and Dinitrosyl Intermediates of FNORs: Semireduction versus Superreduction of NO. *J. Am. Chem. Soc.* **2020**, *142*, 6600-6616.
36. Lehnert, N.; Fujisawa, K.; Camarena, S.; Dong, H. T.; White, C. J. Activation of Non-Heme Iron-Nitrosyl Complexes: Turning up the Heat. *ACS Catal.* **2019**, *9*, 10499-10518.
37. Pal, N.; Jana, M.; Majumdar, A. Reduction of NO by diiron complexes in relation to flavodiiron nitric oxide reductases. *Chem. Commun.* **2021**, *57*, 8682-8698.
38. Jana, M.; Pal, N.; White, C. J.; Kupper, C.; Meyer, F.; Lehnert, N.; Majumdar, A. Functional Mononitrosyl Diiron(II) Complex Mediates the Reduction of NO to N₂O with Relevance for Flavodiiron NO Reductases. *J. Am. Chem. Soc.* **2017**, *140*, 14380-14383.
39. Feig, A. L.; Bautista, M. T.; Lippard, S. J. A Carboxylate-Bridged Non-heme Diiron Dinitrosyl Complex. *Inorg. Chem.* **1996**, *35*, 6892-6898.
40. Zheng, S.; Berto, T. C.; Dahl, E. W.; Hoffman, M. B.; Speelman, A. L.; Lehnert, N. The Functional Model Complex [Fe₂(BPMP)(OPr)(NO)₂](BPh₄)₂ Provides Insight into the Mechanism of Flavodiiron NO Reductases. *J. Am. Chem. Soc.* **2013**, *135*, 4902–4905.
41. Dong, H. T.; White, C. J.; Zhang, B.; Krebs, C.; Lehnert, N. Non-Heme Diiron Model Complexes Can Mediate Direct NO Reduction: Mechanistic Insight into Flavodiiron NO Reductases. *J. Am. Chem. Soc.* **2018**, *140*, 13429-13440.
42. Poptic, A. L.; Klinger, J. K.; Carter, S. L.; Moore, C. E.; Zhang, S. Nitrite Formation at a Diiron Dinitrosyl Complex. *J. Am. Chem. Soc.* **2023**.
43. Gonçalves, V. L.; Vicente, J. B.; Pinto, L.; Romão, C. V.; Frazão, C.; Sarti, P.; Giuffrè, A.; Teixeira, M. Flavodiiron Oxygen Reductase from *Entamoeba histolytica*. *J. Biol. Chem.* **2014**, *289*, 28260-28270.
44. Vicente, J. B.; Teixeira, M. Redox and Spectroscopic Properties of the *Escherichia coli* Nitric Oxide-detoxifying System Involving Flavorubredoxin and Its NADH-oxidizing Redox Partner. *J. Biol. Chem.* **2005**, *280*, 34599-34608.
45. Dong, H. T.; Camarena, S.; Sil, D.; Lengel, M. O.; Zhao, J.; Hu, M. Y.; Alp, E. E.; Krebs, C.; Lehnert, N. What Is the Right Level of Activation of a High-Spin {FeNO}⁷ Complex to Enable Direct N–N Coupling? Mechanistic Insight into Flavodiiron NO Reductases. *J. Am. Chem. Soc.* **2022**, *144*, 16395-16409.
46. Dey, A.; Gordon, J. B.; Albert, T.; Sabuncu, S.; Siegler, M. A.; MacMillan, S. N.; Lancaster, K. M.; Moëne-Loccoz, P.; Goldberg, D. P. A Nonheme Mononuclear {FeNO}⁷ Complex that

Produces N₂O in the Absence of an Exogenous Reductant. *Angew. Chem. Int. Ed.* **2021**, *60*, 21558-21564.

47. Hayashi, T.; Caranto, J. D.; Wampler, D. A.; Kurtz, D. M., Jr.; Moënne-Loccoz, P. Insights into the Nitric Oxide Reductase Mechanism of Flavodiiron Proteins from a Flavin-Free Enzyme. *Biochemistry* **2010**, *49*, 7040–7049.

48. Lu, J.; Bi, B.; Lai, W.; Chen, H. Origin of Nitric Oxide Reduction Activity in Flavo-Diiron NO Reductase: Key Roles of the Second Coordination Sphere. *Angew. Chem. Int. Ed.* **2019**, *58*, 3795-3799.

49. White, C. J.; Lengel, M. O.; Bracken, A. J.; Kampf, J. W.; Speelman, A. L.; Alp, E. E.; Hu, M. Y.; Zhao, J.; Lehnert, N. Distortion of the [FeNO]₂ Core in Flavodiiron Nitric Oxide Reductase Models Inhibits N–N Bond Formation and Promotes Formation of Unusual Dinitrosyl Iron Complexes: Implications for Catalysis and Reactivity. *J. Am. Chem. Soc.* **2022**, *144*, 3804-3820.

50. Dong, H. T.; Zong, Y.; Bracken, A. J.; Lengel, M. O.; Kampf, J. W.; Sil, D.; Krebs, C.; Lehnert, N. Synthesis and characterization of a model complex for flavodiiron NO reductases that stabilizes a diiron mononitrosyl complex. *J. Inorg. Biochem.* **2022**, *229*, 111723.

51. Comba, P.; Gahan, L. R.; Mereacre, V.; Hanson, G. R.; Powell, A. K.; Schenk, G.; Zajaczkowski-Fischer, M. Spectroscopic Characterization of the Active Fe^{III}Fe^{II} and Fe^{III}Fe^I Forms of a Purple Acid Phosphatase Model System. *Inorg. Chem.* **2012**, *51*, 12195-12209.

52. Bernhardt, P. V.; Bosch, S.; Comba, P.; Gahan, L. R.; Hanson, G. R.; Mereacre, V.; Noble, C. J.; Powell, A. K.; Schenk, G.; Wadepohl, H. An Approach to More Accurate Model Systems for Purple Acid Phosphatases (PAPs). *Inorg. Chem.* **2015**, *54*, 7249-7263.

53. CrysAlisPro 1.171.38.41 (Rigaku Oxford Diffraction, 2015).

54. Sheldrick, G. Crystal structure refinement with SHELXL. *Acta Cryst.* **2015**, *C71*, 3-8.

55. Frisch, M. J.; Trucks, G. W.; Schlegel, H. B.; Scuseria, G. E.; Robb, M. A.; Cheeseman, J. R.; Scalmani, G.; Barone, V.; Mennucci, B.; Petersson, G. A.; Nakatsuji, H.; Caricato, M.; Li, X.; Hratchian, H. P.; Izmaylov, A. F.; Bloino, J.; Zheng, G.; Sonnenberg, J. L.; Hada, M.; Ehara, M.; Toyota, K.; Fukuda, R.; Hasegawa, J.; Ishida, M.; Nakajima, T.; Honda, Y.; Kitao, O.; Nakai, H.; Vreven, T.; Montgomery, J. A., Jr.; Peralta, J. E.; Ogliaro, F.; Bearpark, M.; Heyd, J. J.; Brothers, E.; Kudin, K. N.; Staroverov, V. N.; Kobayashi, R.; Normand, J.; Raghavachari, K.; Rendell, A.; Burant, J. C.; Iyengar, S. S.; Tomasi, J.; Cossi, M.; Rega, N.; Millam, J. M.; Klene, M.; Knox, J. E.; Cross, J. B.; Bakken, V.; Adamo, C.; Jaramillo, J.; Gomperts, R.; Stratmann, R. E.; Yazyev, O.; Austin, A. J.; Cammi, R.; Pomelli, C.; Ochterski, J. W.; Martin, R. L.; Morokuma, K.; Zakrzewski, V. G.; Voth, G. A.; Salvador, P.; Dannenberg, J. J.; Dapprich, S.; Daniels, A. D.; Farkas, O.; Foresman, J. B.; Ortiz, J. V.; Cioslowski, J.; Fox, D. J.; Gaussian, Inc.: Wallingford, CT, 2009.

56. Frisch, M. J.; Trucks, G. W.; Schlegel, H. B.; Scuseria, G. E.; Robb, M. A.; Cheeseman, J. R.; Scalmani, G.; Barone, V.; Petersson, G. A.; Nakatsuji, H.; Li, X.; Caricato, M.; Marenich, A. V.; Bloino, J.; Janesko, B. G.; Gomperts, R.; Mennucci, B.; Hratchian, H. P.; Ortiz, J. V.; Izmaylov, A. F.; Sonnenberg, J. L.; Williams; Ding, F.; Lipparini, F.; Egidi, F.; Goings, J.; Peng, B.; Petrone, A.; Henderson, T.; Ranasinghe, D.; Zakrzewski, V. G.; Gao, J.; Rega, N.; Zheng, G.; Liang, W.; Hada, M.; Ehara, M.; Toyota, K.; Fukuda, R.; Hasegawa, J.; Ishida, M.; Nakajima, T.; Honda, Y.; Kitao, O.; Nakai, H.; Vreven, T.; Throssell, K.; Montgomery Jr., J. A.; Peralta, J. E.; Ogliaro, F.; Bearpark, M. J.; Heyd, J. J.; Brothers, E. N.; Kudin, K. N.; Staroverov, V. N.; Keith, T. A.; Kobayashi, R.; Normand, J.; Raghavachari, K.; Rendell, A. P.; Burant, J. C.; Iyengar, S. S.; Tomasi, J.; Cossi, M.; Millam, J. M.;

- Klene, M.; Adamo, C.; Cammi, R.; Ochterski, J. W.; Martin, R. L.; Morokuma, K.; Farkas, O.; Foresman, J. B.; Fox, D. J.; Gaussian 16: Wallingford, CT, 2016.
57. Perdew, J. P. Density-functional approximation for the correlation energy of the inhomogeneous electron gas. *Phys. Rev. B* **1986**, *33*, 8822-8824.
58. Perdew, J. P.; Burke, K.; Wang, Y. Generalized gradient approximation for the exchange-correlation hole of a many-electron system. *Phys. Rev. B* **1996**, *54*, 16533-16539.
59. Wachters, J. H. Gaussian basis set for molecular wavefunctions containing third-row atoms. *J. Chem. Phys.* **1970**, *52*, 1033.
60. Hay, P. J. Gaussian basis sets for molecular calculations - representation of 3D orbitals in transition-metal atoms. *J. Chem. Phys.* **1977**, *66*, 4377-4384.
61. Rassolov, V. A.; Pople, J. A.; Ratner, M. A.; Windus, T. L. 6-31G* basis set for atoms K through Zn. *J. Chem. Phys.* **1998**, *109*, 1223-1229.
62. Schaefer, A.; Horn, H.; Ahlrichs, R. J. Fully optimized contracted Gaussian basis sets for atoms Li to Kr. *J. Chem. Phys.* **1992**, *97*, 2571-2577.
63. Schaefer, A.; Huber, C.; Ahlrichs, R. Fully optimized contracted Gaussian basis sets of triple zeta valence quality for atoms Li to Kr. *J. Chem. Phys.* **1994**, *100*, 5829-5835.
64. Parker, F. S. In *Applications of Infrared Spectroscopy in Biochemistry, Biology, and Medicine*; Springer US: Boston, MA, 1971, p 165-172.
65. Van Stappen, C.; Lehnert, N. Mechanism of N-N Bond Formation by Transition Metal-Nitrosyl Complexes: Modeling Flavodiiron Nitric Oxide Reductases. *Inorg. Chem.* **2018**, *57*, 4252-4269.
66. Tsai, M. L.; Tsou, C. C.; Liaw, W. F. Dinitrosyl Iron Complexes (DNICs): From Biomimetic Synthesis and Spectroscopic Characterization towards Unveiling the Biological and Catalytic Roles of DNICs. *Acc. Chem. Res.* **2015**, *48*, 1184-1193.
67. Butler, A. R.; Megson, I. L. Non-Heme Iron Nitrosyls in Biology. *Chem. Rev.* **2002**, *102*, 1155-1166.
68. Li, L.; Li, L. Recent advances in multinuclear metal nitrosyl complexes. *Coord. Chem. Rev.* **2016**, *306*, 678-700.
69. Tsai, F.-T.; Lee, Y.-C.; Chiang, M.-H.; Liaw, W.-F. Nitrate-to-Nitrite-to-Nitric Oxide Conversion Modulated by Nitrate-Containing {Fe(NO)₂}⁹ Dinitrosyl Iron Complex (DNIC). *Inorg. Chem.* **2013**, *52*, 464-473.
70. Huang, H.-W.; Tsou, C.-C.; Kuo, T.-S.; Liaw, W.-F. New Members of a Class of Dinitrosyliron Complexes (DNICs): Interconversion and Spectroscopic Discrimination of the Anionic {Fe(NO)₂}⁹ [(NO)₂Fe(C₃H₃N₂)₂]⁻ and [(NO)₂Fe(C₃H₃N₂)(SR)]⁻ (C₃H₃N₂ = Deprotonated Imidazole; R = ^tBu, Et, Ph). *Inorg. Chem.* **2008**, *47*, 2196-2204.
71. Kindermann, N.; Schober, A.; Demeshko, S.; Lehnert, N.; Meyer, F. Reductive Transformations of a Pyrazolate-Based Bioinspired Diiron–Dinitrosyl Complex. *Inorg. Chem.* **2016**, *55*, 11538-11550.
72. Bar, A. K.; Heras Ojea, M. J.; Tang, J.; Layfield, R. A. Coupling of Nitric Oxide and Release of Nitrous Oxide from Rare-Earth-Dinitrosyliron Complexes. *J. Am. Chem. Soc.* **2020**, *142*, 4104-4107.

